J. Fluid Mech. (2025), *vol.* 1016, A30, doi:10.1017/jfm.2025.10361

Effects of conjugate heat transfer on large-scale flow structures in convection

Matti Ettel[1], **Philipp P. Vieweg**[2] **and Jörg Schumacher**[1,3]

[1]Institute of Thermodynamics and Fluid Mechanics, Technische Universität Ilmenau, D-98684 Ilmenau, Postfach 100565, Germany

[2]Department of Applied Mathematics and Theoretical Physics, Wilberforce Road, Cambridge CB3 0WA, UK

[3]Tandon School of Engineering, New York University, New York, NY 11021, USA

Corresponding author: Philipp P. Vieweg, ppv24@cam.ac.uk

(Received 28 February 2025; revised 8 May 2025; accepted 12 June 2025)

The constant temperature and constant heat flux thermal boundary conditions, both developing distinct flow patterns, represent limiting cases of ideally conducting and insulating plates in Rayleigh–Bénard convection flows, respectively. This study bridges the gap in between, using a conjugate heat transfer (CHT) set-up and studying finite thermal diffusivity ratios κ_s/κ_f to better represent real-life conditions in experiments. A three-dimensional Rayleigh–Bénard convection configuration including two fluid-confining plates is studied via direct numerical simulations given a Prandtl number $Pr = 1$. The fluid layer of height H and horizontal extension L obeys no-slip boundary conditions at the two solid–fluid interfaces and an aspect ratio of $\varGamma = L/H = 30$ while the relative thickness of each plate is $\varGamma_s = H_s/H = 15$. The entire domain is laterally periodic. Here, different κ_s/κ_f are investigated for moderate Rayleigh numbers $Ra = \left\{10^4, 10^5\right\}$. We observe a gradual shift of the size of the characteristic flow patterns and their induced heat and mass transfer as κ_s/κ_f is varied, suggesting a relation between the recently studied turbulent superstructures and supergranules for constant temperature and constant heat flux boundary conditions, respectively. Performing a linear stability analysis for this CHT configuration confirms these observations theoretically while extending previous studies by investigating the impact of a varying solid plate thickness $\varGamma_s$. Moreover, we study the impact of κ_s/κ_f on both the thermal and viscous boundary layers. Given the prevalence of finite κ_s/κ_f in nature, this work is a starting point to extend our understanding of pattern formation in geo- and astrophysical convection flows.

Key words: Bénard convection, atmospheric flows, pattern formation

---

1. Introduction

Thermal convection – the buoyancy-driven transport of mass and heat – is an omnipresent fluid flow process in nature, occurring not just in geophysical systems like clusters of clouds over the ocean (Mapes & Houze 1993) or the Earth's mantle (Chillà & Schumacher 2012), but also on other planets such as the storms on Jupiter (Young & Read 2017) and Saturn (García-Melendo, Huseo & Sánchez-Lavega 2013) or stars like in the Sun's solar convection zone (Schumacher & Sreenivasan 2020). Understanding this process is thus vital to comprehending geo- and astrophysical flows.

Rayleigh–Bénard convection can be seen as the paradigm of such, containing all essential ingredients and permitting the investigation of even complex convection phenomena like pattern formation in detail. There, fluid is confined between two parallel, horizontally extended plates while being heated from below and cooled from above. When interacting with gravity, an interplay between buoyant and viscous forces occurs which is quantified by the Rayleigh number Ra. Once thermal driving gets strong enough to destabilise the fluid layer – marked by passing the critical Rayleigh number Ra_c – instabilities start growing and convection sets in (Rayleigh 1916).

By virtue of rapid improvements in computational power, it only became possible in recent years to numerically study large-scale pattern formation for extended domains due to the strong scale separation towards the small Kolmogorov or Batchelor scales (Scheel, Emran & Schumacher 2013). Extended fluid domains, i.e. domains possessing a (horizontal) aspect ratio $\varGamma = L/H \gg 1$ where L and H are the horizontal and vertical extent, respectively, are vital for understanding natural systems. Since the influence of lateral boundaries decreases with $O(\varGamma^{-2})$ (Manneville 2006; Cross & Greenside 2009; Koschmieder 2009), it is typically assumed that $\varGamma \gtrsim 20$ lets this impact practically vanish and thus approximates real-life scenarios fairly well (Koschmieder 2009; Stevens *et al.* 2018; Krug, Lohse & Stevens 2020).

Traditionally, the heating and cooling of the fluid has been achieved in two ways: either applying (two different) constant temperatures (i.e. Dirichlet type thermal boundary condition) or a constant heat flux (i.e. Neumann type). Previous studies have found that these thermal boundary conditions govern the pattern formation process, leading to either turbulent superstructures – an arrangement of large-scale convection rolls and cells of size $\varLambda \sim O(H)$ – in the Dirichlet case (Pandey, Scheel & Schumacher 2018; Stevens *et al.* 2018) or a pair of supergranules – two pairs of larger-scale convection rolls $\varLambda \sim \varGamma H \gg O(H)$ that eventually span across the entire domain – in the Neumann case (Vieweg *et al.* 2021, 2022, 2024; Vieweg, 2024*a*). Interestingly, both kinds of these turbulent long-living large-scale flow structures (Vieweg 2023) are reminiscent of the respective critical pattern present at the onset of convection (Rayleigh 1916; Pellew & Southwell 1940; Hurle, Jakeman & Pike 1967).

These two conditions, however, represent mathematically idealised scenarios, which are illustrated in figure 1(*a*). In fact, they omit the vertically adjacent matter or solid that confines and, thus, influences the fluid. Using a conjugate heat transfer (CHT) set-up addresses the problem more holistically by modelling these plates as solid thermal conductors such that not only the heat transfer in the fluid, but also in the adjacent solids as well as their solid–fluid interaction is considered (Perelman 1961). Here, as illustrated in figure 1(*b*), (external) thermal boundary conditions are applied as constant temperatures T_h and T_c at the very bottom and top of the solid plates of relative thickness or vertical aspect ratio $\varGamma_s = H_s/H$, respectively. This causes a temperature gradient within the solid plates before reaching the (internal) thermal boundary conditions at the solid–fluid interfaces – offering the, based on system dynamics, dynamically manifesting temperatures T_b and T_t – where both the temperature and heat flux are coupled between the different subdomains.

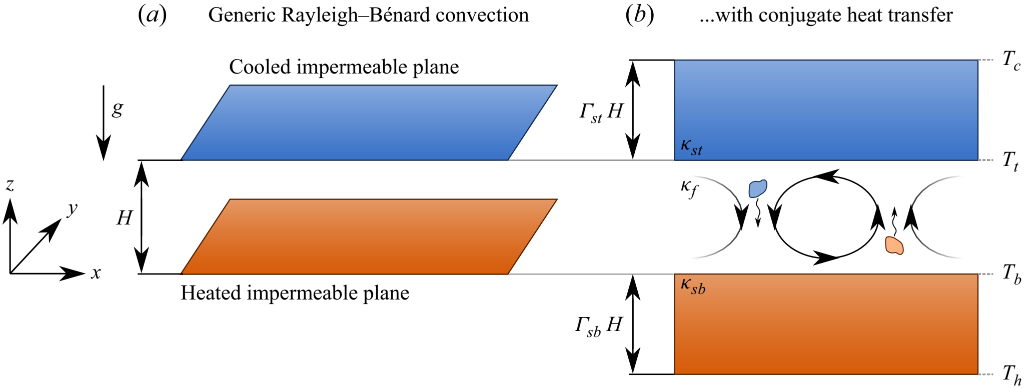

Figure 1. Fundamental configuration. In Rayleigh–Bénard convection, (*a*) a layer of fluid is confined between a heated bottom and a cooled top plane, respectively. While these planes are typically also the limits of the numerical domain, (*b*) this study includes the (otherwise omitted) adjacent plates together with the coupled or conjugate heat transfer (CHT) across the two solid–fluid interfaces. The location of different temperatures is defined on the right while only T_h and T_c are controlled – other temperatures manifest dynamically. In this study, $\kappa_{st} = \kappa_{sb} = \kappa_s$ and $\Gamma_{st} = \Gamma_{sb} = \Gamma_s$.

The ratio of thermal diffusivities between the solids and the fluid, κ_s/κ_f, plays an integral role in governing the aforementioned pattern formation process as the Neumann case is represented by $\kappa_s/\kappa_f \to 0$ whereas the Dirichlet case corresponds to $\kappa_s/\kappa_f \to \infty$. While previous studies in large aspect ratios (Pandey *et al.* 2018; Vieweg *et al.* 2021, 2021*a*, 2022; Schneide *et al.* 2022, 2024, 2025; Vieweg 2023, 2024*a*) have only been focusing on these extreme ends, natural systems always are located somewhere in between. Although some studies of finite κ_s/κ_f have already analysed heat transfer in a CHT set-up experimentally (Vasil'ev *et al.* 2015) or for cylindrical cells of small aspect ratios $\Gamma = 1/2$ (Verzicco 2002, 2004; Foroozani, Krasnov & Schumacher 2021) and others have contrasted the difference in heat transport between the Dirichlet and Neumann cases in small cells (Verzicco & Sreenivasan 2008; Johnston & Doering 2009), the pattern formation process has not yet been investigated. Since both turbulent superstructures (Krug *et al.* 2020) and supergranules (Vieweg, Scheel & Schumacher 2021) are of crucial importance for the induced heat transfer across the fluid layer, a detailed understanding of pattern formation is indispensable. Moreover, the ratio of thermophysical properties between the solid and fluid is crucial beyond our focus on pattern formation aspects, e.g. for the turbulent heat transfer across the fluid layer. This holds particularly for laboratory experiments at very large Rayleigh numbers of $Ra \gtrsim 10^{12}$ where the enhanced turbulence-induced effective conductivity in the fluid can be close to the one in the plates. This requires corrections in Nu, which have been discussed, for example, by Niemela & Sreenivasan (2006).

This study aims to represent natural scenarios of $\kappa_s/\kappa_f \in (0, \infty)$ at a large aspect ratio $\Gamma = 30$ more accurately by considering the coupled or conjugate heat transfer (CHT) at the solid–fluid interfaces, thus coining the term natural thermal boundary conditions. Comprehending this region is crucial to enhancing our understanding of convection flows and their properties in real-life geo- and astrophysical scenarios. To do so, direct numerical simulations are conducted for two Rayleigh numbers $Ra = \{10^4, 10^5\}$ over an array of different κ_s/κ_f. As a primary result of this work, we observe pronounced gradual shifts of both the size of flow structures and their induced heat transfer when varying κ_s/κ_f, underlining the importance of long-living large-scale flow structures as an umbrella term for both turbulent superstructures and supergranules. The transition of large-scale flow structures comes with gradual shifts in both the thermal as well as viscous boundary layer thicknesses. This numerical approach is complemented theoretically by a comprehensive linear stability analysis regarding the onset of convection. This analysis confirms the aforementioned transition between flow structures as a gradual shift towards larger critical wavenumbers k_c is observed when moving from Neumann to Dirichlet conditions. As the vertical aspect ratio or plate thickness $\varGamma_s$ represents an additional free parameter in the CHT set-up, we extend both of our approaches towards a variation of $\varGamma_s$ and find that thin plates stabilise the layer especially for moderate λ_s/λ_f. We remark that this, together with easy-to-handle regression fits, extends the results obtained by Hurle *et al.* (1967) for infinitely thick plates. The present study bridges the gap between classical thermal boundary conditions by incorporating solid subdomains together with the coupled temperatures and heat transfers at the solid–fluid interfaces, allowing us to interpret natural flows in the geo- and astrophysical context more successfully.

2. Governing equations and numerical method

2.1. *Governing equations*

We consider an incompressible flow based on the Oberbeck–Boussinesq approximation (Oberbeck 1879; Boussinesq 1903). This means that all material parameters are constant – except for the mass density, the latter of which varies at first order with temperature when interacting with gravity only. The three-dimensional equations of motion are non-dimensionalised based on the fluid layer height H and the temperatures at the bottom and top of this fluid layer, T_b and T_t (see also figure 1*b*), respectively. We use the spatiotemporal average of these temperature fields to define the characteristic (dimensional) temperature scale $\Delta T := \langle T_b - T_t \rangle_{A,t}$ where A denotes the entire horizontal cross-section. Note that this implies a non-dimensionalisation $T = \Delta T\, \tilde{T}$ together with the assumption of a resulting non-dimensional temperature difference across the fluid layer of $\Delta T_N := \langle \tilde{T}_b - \tilde{T}_t \rangle_{A,t} \equiv 1$. We stress explicitly that we write out the tildes here to clearly distinguish the dimensional ΔT and non-dimensional temperature difference ΔT_N but will, from now on, mostly omit such for better readability. By virtue of the free-fall inertia balance, the free-fall velocity $U_f = \sqrt{\alpha g \Delta T H}$ and time scale $\tau_f = H/U_f = \sqrt{H/\alpha g \Delta T}$ can be acquired where α is the volumetric thermal expansion coefficient of the fluid at constant pressure, g the acceleration due to gravity and $\rho_{ref,f}$ the reference density of the fluid at reference temperature. We solve the resulting coupled equations using the spectral-element solver Nek5000 (Fischer 1997; Scheel *et al.* 2013).

For the fluid subdomain, the governing equations are

$$\nabla \cdot \boldsymbol{u} = 0, \tag{2.1}$$

$$\frac{\partial \boldsymbol{u}}{\partial t} + (\boldsymbol{u} \cdot \nabla)\, \boldsymbol{u} = -\nabla p + \sqrt{\frac{Pr}{Ra}} \nabla^2 \boldsymbol{u} + T \boldsymbol{e}_z, \tag{2.2}$$

$$\frac{\partial T}{\partial t} + (\boldsymbol{u} \cdot \nabla)\, T = \frac{1}{\sqrt{Ra\, Pr}} \nabla^2 T. \tag{2.3}$$

In contrast, the solid subdomains require us to solve a pure diffusion equation

$$\frac{\partial T}{\partial t} = \frac{\kappa_s}{\kappa_f} \frac{1}{\sqrt{Ra\, Pr}} \nabla^2 T \tag{2.4}$$

only (Foroozani *et al.* 2021; Vieweg *et al.* 2025). Here, $\boldsymbol{u}$, T and p represent the (non-dimensional) velocity, temperature and pressure fields, whereas $\kappa_\varPhi = \lambda_\varPhi / \rho_{ref,\varPhi} c_{p,\varPhi}$ is the thermal diffusivity. Its ratio between the solid and fluid domains κ_s/κ_f constitutes an important control parameter over the course of this work, with the subscripts $\varPhi = \{f, s\}$

denoting the fluid and solid, respectively. Here λ_Φ represents the thermal conductivity, $\rho_{ref,\Phi}$ the mass density and $c_{p,\Phi}$ the specific heat capacity at constant pressure. Furthermore, the Rayleigh and Prandtl number are defined via

$$Ra = \frac{\alpha g \Delta T H^3}{\nu_f \kappa_f} \quad \text{and} \quad Pr = \frac{\nu_f}{\kappa_f}, \tag{2.5}$$

where ν_f is the kinematic viscosity of the fluid . Note that (2.4) holds for both the top and bottom plate – as they will offer identical thermal diffusivities – and, thus, differs from our recent work (Vieweg *et al.* 2025).

2.2. *Numerical domain, boundary and initial conditions*

These governing equations are complemented by a numerical domain and its respective boundary conditions. We define the horizontal extent L of our numerical domain by the (horizontal) aspect ratio $\Gamma := L/H$, whereas the vertical aspect ratio $\Gamma_s := H_s/H$ describes the thickness of each of the surrounding solid plates. Note that both of these aspect ratios are based on the height H of the fluid domain, whereas any subdomain offers the square horizontal cross-section $A = \Gamma \times \Gamma$. Regarding figure 1, the solid bottom and top domains are thus situated at $z \in [-\Gamma_s, 0]$ and $z \in [1, 1 + \Gamma_s]$, respectively, with the fluid in between at $z \in [0, 1]$.

We consider a horizontally periodic domain where any quantity $\boldsymbol{\Phi}$ repeats according to

$$\boldsymbol{\Phi}\left(\boldsymbol{x}\right) = \boldsymbol{\Phi}\left(\boldsymbol{x} + i_x L_x \boldsymbol{e}_x + i_y L_y \boldsymbol{e}_y\right), \quad i_{x,y} \in \mathbb{N} \tag{2.6}$$

and offers no-slip boundary conditions

$$\boldsymbol{u}\left(z = \{0, 1\}\right) = \boldsymbol{0} \tag{2.7}$$

at both solid–fluid interfaces. Thermal boundary conditions are applied in the form of constant temperatures at the very top and bottom of the plates (i.e. $z = \{-\Gamma_s, 1 + \Gamma_s\}$) which will further be referred to as

$$T\left(z = -\Gamma_s\right) = T_h \quad \text{and} \tag{2.8}$$

$$T\left(z = 1 + \Gamma_s\right) = T_c. \tag{2.9}$$

By nature of the CHT set-up, temperature fields and diffusive heat fluxes are coupled at the solid–fluid interfaces (i.e. $z = \{0, 1\}$) according to

$$T_b := T_f\left(z = 0\right) = T_s\left(z = 0\right), \quad \frac{\lambda_s}{\lambda_f} \left.\frac{\partial T_s}{\partial z}\right|_{z=0} = \left.\frac{\partial T_f}{\partial z}\right|_{z=0}, \tag{2.10}$$

$$T_t := T_f\left(z = 1\right) = T_s\left(z = 1\right), \quad \frac{\lambda_s}{\lambda_f} \left.\frac{\partial T_s}{\partial z}\right|_{z=1} = \left.\frac{\partial T_f}{\partial z}\right|_{z=1}. \tag{2.11}$$

Note that while the energy equation (2.4) contains κ_s/κ_f due to the non-dimensionalisation, the boundary conditions (2.10) and (2.11) include the ratio λ_s/λ_f to match the diffusive heat fluxes at the interfaces. In order to avoid another control parameter, we assume in our simulations $\rho_s c_{p,s}/\rho_f c_{p,f} = 1$ such that $\lambda_s/\lambda_f \equiv \kappa_s/\kappa_f$ follows. We will thus use κ_s/κ_f as the control parameter for the discussions in the main text, except for the linear stability analysis. We additionally stress that as we fix the externally applied temperatures T_h and T_c, see again (2.8) and (2.9), the resulting temperature fields at the solid–fluid interfaces T_b and T_t vary in both space and time by virtue of the systems dynamics.

The ratio κ_s/κ_f strongly impacts the way in which the fluid interacts with the solid and *vice versa*. For $\kappa_s/\kappa_f \to \infty$, the Dirichlet case is resembled where the temperatures at the solid–fluid interfaces become constant (since the solid is a much better thermal conductor).

Setting	Solid/Fluid	κ_s/κ_f	λ_s/λ_f
Ocean	Seawater/air	5.71×10^{-3}	22.8
Mountain (Dolomites)	Dolomite/air	1.16×10^{-1}	220
Beach	Quartz/air	2.20×10^{-1}	352

Table 1. Ratios of thermophysical properties in natural configurations. Values of both the thermal diffusivity as well as thermal conductivity are taken at 10 °C for seawater (salinity of 35 p.p.t.), air and quartz from Ochsner (2019), Ibrahim & Badawy (2017), and for dolomite from Stout & Robie (1963) and Horai (1971).

In contrast, for $\kappa_s/\kappa_f \rightarrow 0$ the Neumann case is mimicked where the vertical temperature gradient becomes constant at these interfaces (since thermal resistance through the fluid is smaller compared with the solid). A more elaborate explanation is provided in Appendix B. In this study, bridging the gap between Dirichlet and Neumann conditions, we are interested in a broad range of κ_s/κ_f centred around unity. Table 1 includes this ratio for a variety of natural configurations and shows that natural flows tend to offer $\kappa_s/\kappa_f \sim O(10^{-3} \ldots 10^{-1})$.

Concerning our initial condition, we follow the procedure described and introduced by Vieweg *et al.* (2025). In a nutshell, we initialise each simulation with a fluid at rest, i.e. $\boldsymbol{u}(\boldsymbol{x}, t = 0) = 0$, and linear temperature profiles which respect the internal boundary conditions between the different subdomains as outlined in (2.10) and (2.11). By adding some tiny random thermal noise $0 \le \Upsilon \le 10^{-3}$, we accelerate the transition to the statistically stationary state under the assumption of an initial Nusselt number $Nu(t = 0) > 1$ based on preliminary simulation runs.

The required, externally applied temperatures T_h and T_c (see (2.8) and (2.9)) are determined as follows. First, we define the global Nusselt number

$$Nu(t) := \frac{\langle (\boldsymbol{J}_{dif} + \boldsymbol{u}T) \boldsymbol{\cdot} \boldsymbol{e}_z \rangle_{V_f}}{\langle \boldsymbol{J}_{dif} \boldsymbol{\cdot} \boldsymbol{e}_z \rangle_{V_f}} = \left\langle -\frac{\partial T}{\partial z} \right\rangle_{V_f} + \left\langle \sqrt{Ra\,Pr}\, u_z T \right\rangle_{V_f}$$
$$= 1 + \sqrt{Ra\,Pr}\, \langle u_z T \rangle_{V_f}\,, \tag{2.12}$$

as a measure of the induced amplification of the global heat transfer due to convective fluid motion. Note that the latter is associated with $\boldsymbol{u}T$ and in contrast to the diffusive heat current $\boldsymbol{J}_{dif}$ while $V_f = A \times H$ represents the fluid volume (Otero *et al.* 2002; Vieweg 2023). Second, given the linear conduction profiles outlined in (Vieweg *et al.* 2025) and an assumed amplification of heat transfer as measured by Nu, it is possible to estimate these applied temperatures – that are required to achieve $\Delta T_N \approx 1$ – according to

$$T_h = 1 + \frac{\lambda_f}{\lambda_s} \Gamma_s Nu \quad \text{and} \quad T_c = -\frac{\lambda_f}{\lambda_s} \Gamma_s Nu. \tag{2.13}$$

Note that, as the final Nu is not known *a priori*, either preliminary two- and three-dimensional simulation runs or our introduced tanh-relationship (which will be discussed in § 4) have been used to find appropriate values for T_h and T_c.

3. Linear stability analysis of the coupled system

Flow structures at the onset of convection, as derivable analytically via a linear stability analysis, are a characteristic of the dynamical system and, thus, helpful for understanding even turbulent flow structures (Pandey *et al.* 2018; Vieweg *et al.* 2021). Although such a linear stability analysis yields a relation $Ra(k)$, it is the global minimum of this function that determines the critical Rayleigh number Ra_c and critical wavenumber k_c. If $Ra \gtrsim Ra_c$, linear perturbations grow exponentially over time and lead to the associated size or wavelength of the emerging flow structures of $\lambda_c = 2\pi / k_c$.

While, given our no-slip boundary conditions, (Ra_c, k_c) are well known for the Dirichlet ($Ra_c = 1707.8$, $k_c = 3.13$) (Pellew & Southwell 1940) and Neumann ($Ra_c = 6! = 720$, $k_c = 0$) (Hurle *et al.* 1967) cases, these values change for vertically infinitely extended (i.e. $\varGamma_s \to \infty$) CHT set-ups with finite ratios of thermal conductivities $\lambda_s/\lambda_f \in (0, \infty)$ (Hurle *et al.* 1967). One can expect that a finite plate thickness $\varGamma_s$ adds an additional layer of complexity.

This study extends the work of Hurle *et al.* (1967) by (i) investigating a broader range of λ_s/λ_f, (ii) considering even finite plate thicknesses $\varGamma_s$ (in § 6) and (iii) deriving easy-to-handle relationships between Ra_c, k_c and λ_s/λ_f.

In order to determine the neutral stability curve and subsequently derive Ra_c as well as k_c, a system of four equations needs to be solved where the determinant of the coefficient matrix $\boldsymbol{M_E}$ is set to zero to obtain a non-trivial solution,

$$\det \boldsymbol{M_E} \overset{!}{=} 0 = \begin{vmatrix} 0 & 1 & 1 & 1 \\ 0 & q_1 t_1 & q_2 t_2 & q_3 t_3 \\ -\frac{\lambda_f}{\lambda_s} \tanh\left(k\varGamma_s\right) & \gamma & -\frac{\gamma}{2}\left(1 - \mathrm{i}\sqrt{3}\right) & -\frac{\gamma}{2}\left(1 - \mathrm{i}\sqrt{3}\right) \\ k & \gamma q_1 t_1 & -\frac{\gamma}{2}\left(1 - \mathrm{i}\sqrt{3}\right) q_2 t_2 & -\frac{\gamma}{2}\left(1 - \mathrm{i}\sqrt{3}\right) q_3 t_3 \end{vmatrix} . \tag{3.1}$$

In the following, we only regard the case of even modes as it provides the lower values for Ra_c. A detailed derivation – explaining all involved variables – is provided in Appendix A.

Figure 2(*a*) contrasts different resulting neutral stability curves for different λ_s/λ_f given $\varGamma_s \to \infty$. Remember that the extreme cases $\lambda_s/\lambda_f = \left\{10^{-6}, 10^{6}\right\}$ mimic the Neumann and Dirichlet cases, respectively, and with which they correspond (Pellew & Southwell 1940; Chandrasekhar 1981; Takehiro *et al.* 2002). Interestingly, after having solved (3.1) for a large number of λ_s/λ_f, we find a gradual and monotonic transition for both Ra_c and k_c in between these extreme conditions as visualised in figure 2(*b*–*d*). Our analysis shows that the onset of convection is generally delayed (i.e. larger Ra_c) with smaller emerging flow structures (i.e. larger k_c) for relatively better solid thermal conductors (i.e. increasing λ_s/λ_f). As highlighted by the inset in figure 2(*b*), $k_c(\lambda_s/\lambda_f)$ exhibits different asymptotic convergence behaviours for the extremes of λ_s/λ_f: While $k_c \sim \lambda_s/\lambda_f^{1/3}$ for $\lambda_s/\lambda_f \to 0$, $k_c \simeq 3.13 = \text{const.}$ for $\lambda_s/\lambda_f \to \infty$. Interestingly, the inflection point is around $\lambda_s/\lambda_f \approx 10^{-3/4}$ (rather than 10^{0}) and thus introduces an asymmetry with respect to λ_s/λ_f.

These (true) solutions are the result of solving (3.1). In order to provide handier solutions that are more accessible, we apply tanh- or polynomial-based regressions to the original data from figure 2(*b*–*d*) and include them therein. Given the parameters shown in table 2, such simple regression fits approximate the true solutions (very) well.

Albeit this linear stability analysis is based on $\varGamma_s \to \infty$, we find that its solutions practically coincide with our numerically employed finite case $\varGamma_s = 15$ as shown in § 6.

4. Nonlinear pattern formation

4.1. *Conducted simulations and pattern formation process*

In order to systematically investigate the impact of natural thermal boundary conditions on convection flows beyond their onset, we conduct two main series of simulations at two Ra varying κ_s/κ_f across a broad range. For all these simulations, the Prandtl number $Pr = 1$,

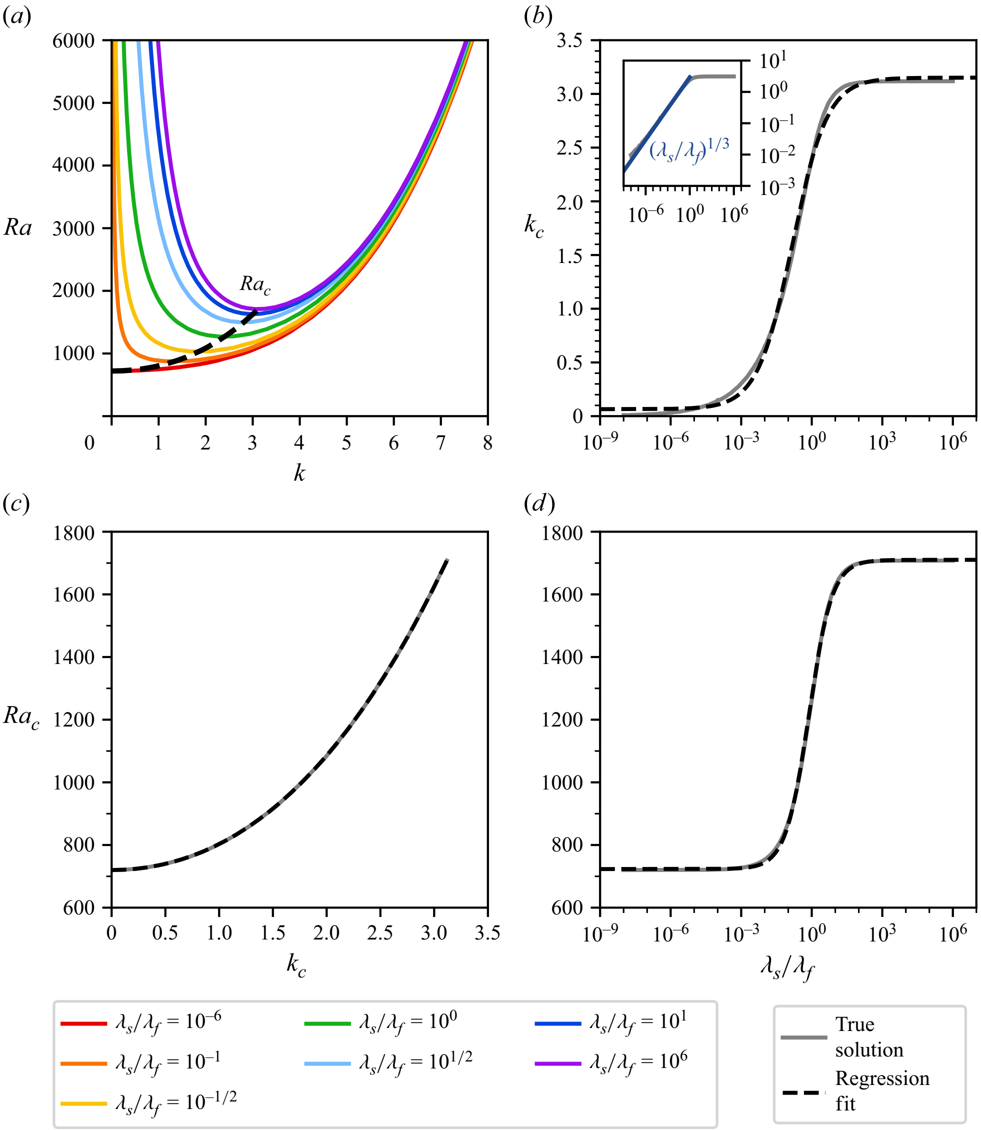

Figure 2. Linear stability of CHT-driven Rayleigh–Bénard convection. The combination of thermophysical properties controls both the general stability (Ra_c) as well as the size of the critical flow structures (k_c). (*a*) Different neutral stability curves indicate (*c*) a gradual and monotonic transition of both Ra_c and k_c (see also panels (*d*) and (*b*), respectively). The true solutions from panels (*b–d*) can be approximated well by tanh- or polynomial-based regressions using parameters described by table 2. Note the different convergence behaviour of k_c for $\lambda_s/\lambda_f \to \infty$ ($k_c = \text{const.}$) and $\lambda_s/\lambda_f \to 0$ ($k_c \sim (\lambda_s/\lambda_f)^{1/3}$) as highlighted by the inset in panel (*b*), the latter of which plots the data double-logarithmically instead.

horizontal aspect ratio $\Gamma = 30$ and vertical aspect ratio $\Gamma_s = 15$. Our choice of such a horizontally extended domain makes the heat and momentum transfer, as quantified by Nu and Re, independent of Γ (Stevens *et al.* 2018) and delays limiting the pattern formation process by the horizontal extent of the domain (Stevens *et al.* 2018; Krug *et al.* 2020; Vieweg 2023) as further discussed in § 4.3. We report a third series of simulations at different Γ_s given $\kappa_s/\kappa_f = 10^0$ in § 6 whereas we contrast extreme cases of κ_s/κ_f with their plateless classical representatives in Appendix B.

f	a	b	c	d	e	R^2	Range of applicability
$k_c(\lambda_s/\lambda_f)$	1.543	0.293	0.554	1.608	–	0.9985	$\lambda_s/\lambda_f \in [0, \infty)$
$Ra_c(\lambda_s/\lambda_f)$	493.546	0.441	0.122	1216.713	–	0.9999	$\lambda_s/\lambda_f \in [0, \infty)$
$Ra_c(k_c)$	0.341	7.576	74.868	0.234	719.996	1.0000	$k_c \in [0, 3.13]$

Table 2. Regression parameters for k_c and Ra_c. A tanh-fit of the form $f(\lambda_s/\lambda_f, Ra) = a \tanh[b\ln(\lambda_s/\lambda_f) + c] + d$ is applied to the values in figure 2 (*a,b*). For $Ra_c(k_c)$ in figure 2(c), a fourth-order polynomial fit of the form $f(k_c) = ak_c^4 + bk_c^3 + ck_c^2 + dk_c + e$ is applied. Here R^2 is the coefficient of determination (Wright 1921) and underlines the quality of these fits.

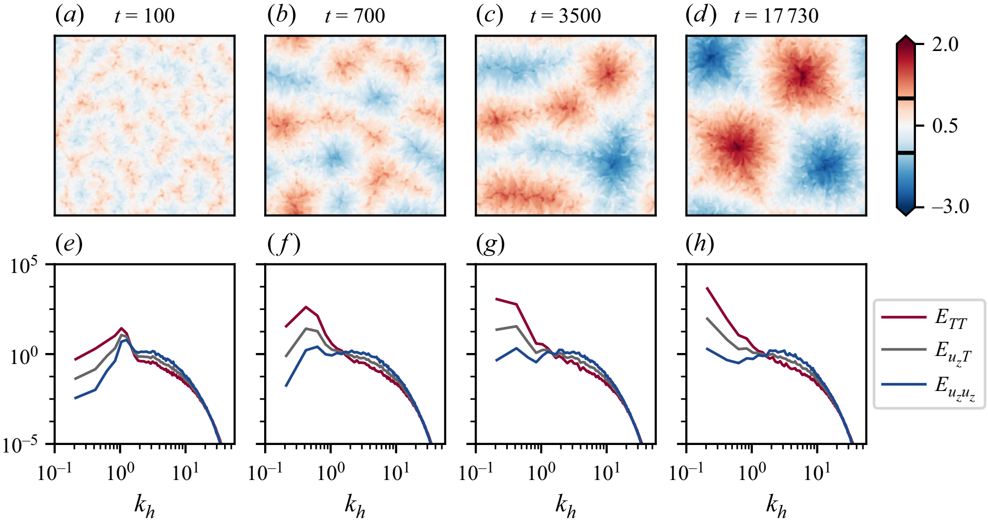

Figure 3. Gradual pattern formation. (*a*) At early times, large-scale granulated flow structures emerge that (*b,c*) gradually merge and form even larger supergranules before (*d*) a statistically stationary state is reached. Here we visualise the thermal footprint $T(x, y, z = 0.5, t)$ of these flow structures. (*e–h*) The corresponding azimuthally averaged Fourier energy spectra (of various fields) highlight a gradual shift of spectral energy towards larger horizontal scales. This shift is governed by κ_s/κ_f, as $\kappa_s/\kappa_f \to 0$, more energy accumulates at even smaller k_h. In contrast to the idealised Neumann case – compare with (Vieweg *et al.* 2021) – the growth of the supergranules stops in this CHT set-up of $Ra = 10^5$ and $\kappa_s/\kappa_f = 10^0$ (Case C5c) before reaching domain size.

Convective pattern formation is known to be a gradual process which reaches statistically stationary flow structures only after a long time, potentially even $O(10^4\tau_f)$ or longer (Vieweg *et al.* 2021, 2022, 2024; Vieweg 2023, 2024*a*). Figure 3 illustrates this process for one of our present CHT cases: at the beginning, granulated flow structures manifest that merge over time towards larger structures. While figure 3(*a–c*) depict the transient regime, figure 3(*d*) illustrates the flow structures by means of their thermal footprint at their statistically stationary state. Reaching this late regime has successfully been probed using different measures such as the integral length scale (Parodi *et al.* 2004; Vieweg *et al.* 2022)

$$\Lambda_T\ (z = 0.5, t) := 2\pi \frac{\int_{k_h} \left[E_{TT}/k_h\right] \mathrm{d}k_h}{\int_{k_h} E_{TT} \mathrm{d}k_h} \tag{4.1}$$

with $E_{TT} \equiv E_{TT}(k_h, z = 0.5, t)$ representing the azimuthally averaged Fourier energy spectrum of the temperature field and k_h the horizontal wavenumber, or the thermal variance (Vieweg *et al.* 2022)

$$\Theta_{rms}(t) := \sqrt{\langle \Theta^2 \rangle_V} \quad \text{with} \quad \Theta(\boldsymbol{x}, t) := T(\boldsymbol{x}, t) - T_{lin}(z) \tag{4.2}$$

where Θ_{rms} is the temperature deviation field around the mean linear conduction profile $T_{lin} = 1 - z$ across the fluid domain (Vieweg 2023, 2024*a*). In case of Neumann-type thermal boundary conditions, Λ_T usually converges more quickly than Θ_{rms} (Vieweg 2023).

Figure 3(*e–h*) demonstrate how various azimuthally averaged Fourier energy spectra develop over the course of this gradual aggregation process. Here, given $E_{\Phi_1\Phi_2} := \langle 1/2\,\mathrm{Re}(\hat{\Phi}_1 \hat{\Phi}_2^*)\rangle_\phi$ with the Fourier coefficients $\hat{\Phi} \equiv \hat{\Phi}(\boldsymbol{k}_h, z, t)$ and azimuthal angle ϕ, we include the averaged spectra associated with the temperature field E_{TT}, vertical convective heat flux E_{u_zT} and vertical velocity $E_{u_zu_z}$ as a function of the absolute horizontal wavenumber k_h. As pattern formation progresses, spectral energy shifts towards smaller k_h – i.e. larger structures – across all of these spectra, thereby underlining the increasing dominance of large-scale flow structures. However, in comparison with the Neumann case described in Vieweg *et al.* (2021) or Vieweg (2023), the aggregation process in the CHT set-up may cease before reaching the domain size – depending on κ_s/κ_f. This dependence between the final size of flow structures (as quantified by Λ_T, see again (4.1)) and κ_s/κ_f will be analysed in more detail in § 4.3.

In this work, due to the inclusion of solid subdomains and thus the two solid–fluid interfaces, we complement the above measures by the dynamically manifesting temperature drop ΔT_N across the fluid layer. We find that this measure requires similar time scales of convergence with particularly large times observed for moderate $\kappa_s/\kappa_f \in [10^{-1}, 10^{1/2}]$. Note that we always require the temperature drop across the fluid layer $\Delta T_N \simeq 1$ (so the non-dimensionalisation for (2.1)–(2.4) holds) whereas the temperature drop across each solid plate $(T_h - T_c - 1)/2$ depends strongly on κ_s/κ_f.

Starting from initial conditions as described in § 2.2, we run each numerical simulation as long as necessary to reach the late statistically stationary regime (probed by Λ_T, Θ_{rms} and ΔT_N) and cover the latter for an extended period of time. Table 3 summarises the simulation parameters for all of our simulation runs.

Figure 4 underlines the increased complexity of these simulations due to the added solid subdomains and their coupled interaction with the fluid layer. While we apply Dirichlet-type fixed temperatures at the very top and bottom of the domain – see figure 4(*a*,*d*) – the local heat flux at these planes may vary in space and time as visualised in figure 4(*e*,*h*). The coupled heat transfer at the two solid–fluid interfaces implies that we control neither the temperature nor the local heat flux (see figures 4(*b*,*c*) or 4(*f*,*g*), respectively) allowing for significantly weaker constraints on the dynamical fluid system. Interestingly, we find the vertical temperature gradient fields not only to be strongly negatively correlated across the fluid layer (i.e. between planes $z_0 = \{0, 1\}$) but also across the entire solid–fluid–solid domain (i.e. between planes $z_0 = \{-\Gamma_s, 1 + \Gamma_s\}$) despite $\Gamma_s = 15$. The temperature fields, on the other hand, appear to be shifted from generally warmer temperatures at $z_0 = 0$ to colder ones at $z_0 = 1$ while still showing the footprint of the underlying flow structures. This underlines the pronounced interplay between solid thermal capacities and the fluid flow.

4.2. *Convective flow patterns for different κ_s/κ_f*

We start by resembling the classical, well-known Neumann- (Vieweg *et al.* 2021; Vieweg 2023) and Dirichlet-type (Pandey *et al.* 2018; Vieweg *et al.* 2021) thermal

Identifier	Ra	κ_s/κ_f	Γ_s	N_e	N	t_r	$(T_h - T_c - 1)/2$
N4	10^4	$\to 0$	15	$100^2 \times 4$	7	10 200	–
C4N	10^4	10^{-6}	15	$100^2 \times (4+2\times 30)$	7	8850	47.5×10^6
C4a	10^4	10^{-1}	15	$100^2 \times (4+2\times 30)$	7	22 950	445.70
C4b	10^4	$10^{-1/2}$	15	$100^2 \times (4+2\times 30)$	7	16 100	128.25
C4c	10^4	10^0	15	$100^2 \times (4+2\times 30)$	7	12 000	36.50
C4d	10^4	$10^{1/4}$	15	$100^2 \times (4+2\times 30)$	7	6100	19.90
C4e	10^4	$10^{1/2}$	15	$100^2 \times (4+2\times 30)$	7	10 100	10.90
C4f	10^4	$10^{3/4}$	15	$100^2 \times (4+2\times 30)$	7	2900	6.14
C4g	10^4	10^1	15	$100^2 \times (4+2\times 30)$	7	6500	3.45
C4D	10^4	10^6	15	$100^2 \times (4+2\times 30)$	7	8140	0.00
D4	10^4	$\to \infty$	15	$100^2 \times 4$	7	10 550	–
N5	10^5	$\to 0$	15	$100^2 \times 4$	11	7000	–
C5a	10^5	10^{-1}	15	$100^2 \times (4+2\times 30)$	11	9030	730.00
C5b	10^5	$10^{-1/2}$	15	$100^2 \times (4+2\times 30)$	11	16 530	227.37
C5c	10^5	10^0	15	$100^2 \times (4+2\times 30)$	11	17 730	70.00
C5d	10^5	$10^{1/4}$	15	$100^2 \times (4+2\times 30)$	11	5530	38.91
C5e	10^5	$10^{1/2}$	15	$100^2 \times (4+2\times 30)$	11	10 030	21.54
C5f	10^5	$10^{3/4}$	15	$100^2 \times (4+2\times 30)$	11	3030	12.09
C5g	10^5	10^1	15	$100^2 \times (4+2\times 30)$	11	4530	6.71
D5	10^5	$\to \infty$	15	$100^2 \times 4$	11	3000	–
C5cG1	10^5	10^0	1	$100^2 \times (4+2\times 4)$	11	8530	4.70
C5c	10^5	10^0	15	$100^2 \times (4+2\times 30)$	11	17 730	70.00
C5cG30	10^5	10^0	30	$100^2 \times (4+2\times 45)$	11	20 030	140.30

Table 3. Simulation parameters. The Prandtl number $Pr=1$ in a horizontally periodic domain of (horizontal) aspect ratio $\Gamma=30$ and no-slip conditions at the two solid–fluid interfaces. The table contains beside the identifier further the Rayleigh number Ra, the thermal diffusivity ratio κ_s/κ_f, the vertical aspect ratio (or thickness) Γ_s of each of the two adjacent solid plates, the total number of spectral elements $N_e=N_{e,x}\times N_{e,y}\times (N_{e,z,f}+2\times N_{e,z,s})$, the polynomial order N of each spectral element, the total simulation runtime t_r and the applied mean temperature drop across each solid plate $(T_h - T_c - 1)/2$.

boundary conditions using our CHT set-up subjected to the extreme $\kappa_s/\kappa_f = \{10^{-6}, 10^6\}$. Appendix B contrasts the resulting flow structures – which are commonly distinguished, respectively, as supergranules (Vieweg *et al.* 2021) and turbulent superstructures (Pandey *et al.* 2018) (or spiral defect chaos for this lower Ra) – and confirms a convergence of the flow for plateless and CHT configurations.

Bridging the gap between these previously studied idealised conditions, figure 5 visualises snapshots of our simulations applying natural thermal boundary conditions covering the range $10^{-1} \leqslant \kappa_s/\kappa_f \leqslant 10^1$. Our simulations show that smaller κ_s/κ_f lead gradually to increased flow structures given a sufficiently extended domain. In our case, the growth of the flow structures is limited by the numerically finite horizontal domain size $\Gamma = 30$ at $\kappa_s/\kappa_f = 10^{-1/2}$ and below. Although we study a limited range of κ_s/κ_f around unity only, it is sufficient to indicate the clear convergence towards either supergranules or turbulent superstructures. This gradual transition from one of the latter to the other suggests covering them both under the umbrella term of long-living large-scale flow structures. Our numerical results for $Ra \gg Ra_c$ are in line with the general, monotonic trend suggested by the linear stability analysis from § 3. Independently of κ_s/κ_f, we find that a larger Ra introduces stronger turbulence on smaller scales including the granular scale (Vieweg *et al.* 2021; Vieweg 2023).

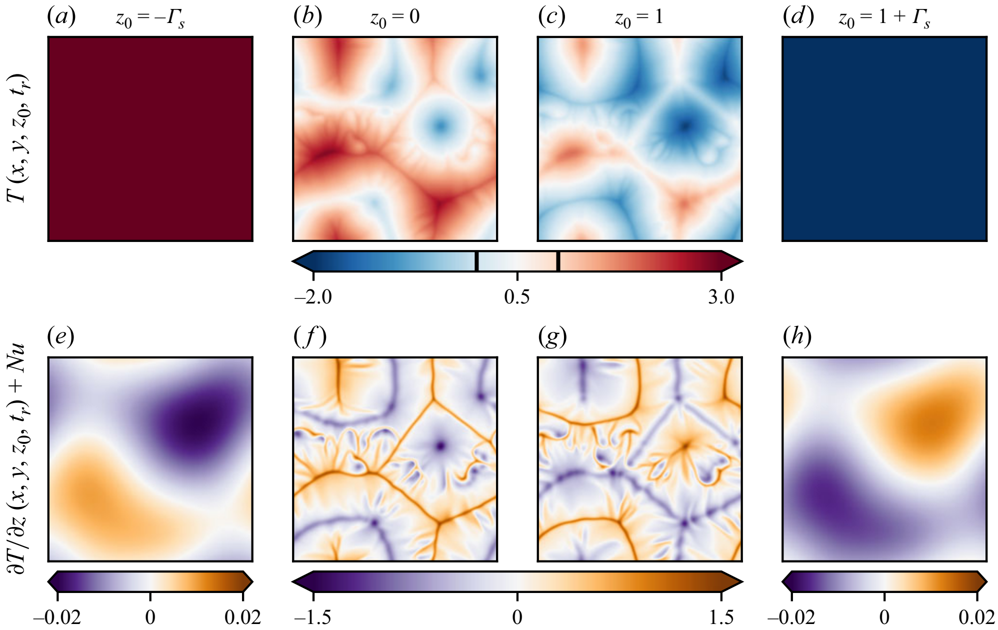

Figure 4. Conjugate heat transfer. In the coupled system, both the temperature (*a*–*d*) and heat flux (*e*–*h*) are coupled at the two solid–fluid interfaces (*b,c,f,g*) while only the temperature field is controlled at the very bottom (*a*) and top (*d*). The respective local heat flux (*e,h*) is still correlated. Here $Ra = 10^5$, $\Gamma_s = 15$, and $\kappa_s/\kappa_f = 10^0$ (i.e. case C4c). Note that when $\kappa_s/\kappa_f \rightarrow \infty$ or $\kappa_s/\kappa_f \rightarrow 0$, either (*b,c*) or (*f,g*) become constant, respectively.

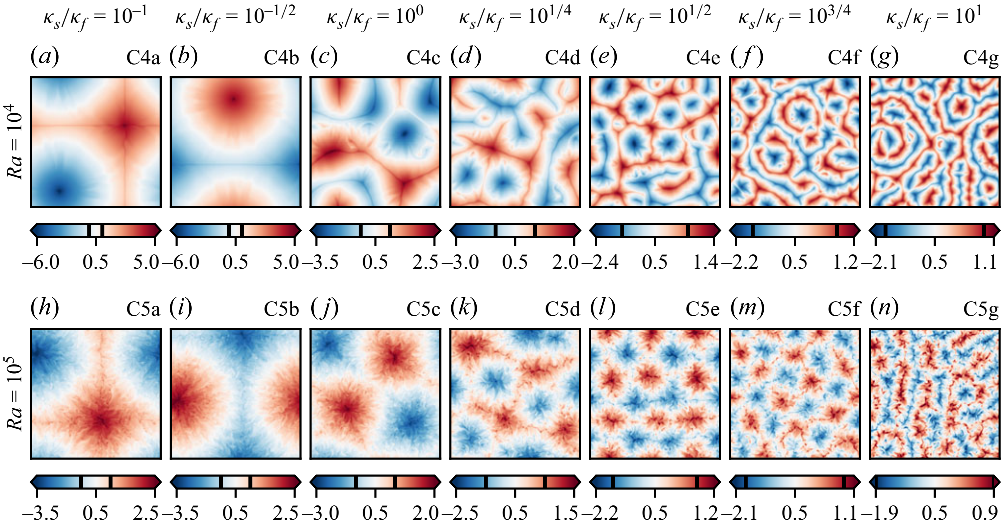

Figure 5. Nonlinear pattern formation. Worse solid thermal conductors (relative to the fluid) lead to the formation of larger flow structures. Here we visualise the instantaneous temperature fields $T\,(x, y, z = 0.5, t = t_{\mathrm{r}})$ given $\Gamma_s = 15$. Identifiers for the runs (see the top-right of each panel) are listed in table 3.

4.3. *Quantitative analysis of convective flow patterns*

We proceed by quantifying selected aspects of our flow structures as well as their induced statistical properties. Firstly, we measure the strength of appearing thermal inhomogeneities at the two solid–fluid interfaces based on both the instantaneous maximum horizontal temperature difference

$$\max\left(\varLambda_h T\right)(t) := \max_{x,y}\left(T\right) - \min_{x,y}\left(T\right) \tag{4.3}$$

and the standard deviation $\mathrm{std}(T)$ for $T \in \{T_b, T_t\}$. This is complemented by the induced global momentum transfer as measured by the Reynolds number (Scheel & Schumacher 2017)

$$Re(t) := \sqrt{\frac{Ra}{Pr}}\, u_{rms} \quad \text{with} \quad u_{rms} := \sqrt{\left\langle \boldsymbol{u}^2 \right\rangle_V}. \tag{4.4}$$

Thirdly, we measure the size or horizontal extent of flow structures based on the integral length scale $\varLambda_T$ as defined in (4.1).

Table 4 summarises the temporal averages and associated temporal standard deviations for all our simulations. Note that this analysis covers an extended period t_{ss} of the late statistically stationary regime of pattern formation rather than a single snapshot.

We remark that reaching exactly $\Delta T_N = 1$ is not possible in a CHT set-up – although being assumed in our non-dimensionalisation, see again § 2.1 – affecting in turn the Rayleigh number as defined in (2.5) and thus also Nu and Re from (2.12) and (4.4), respectively. Therefore, the achieved Nusselt and Reynolds numbers have been corrected by this error $\delta T = \Delta T_N - 1$ according to

$$Re = \frac{Re^a}{\sqrt{\Delta T_N}} = \frac{Re^a}{\sqrt{1+\delta T}} \sim \delta T^{-1/2} \quad \text{and} \quad Nu = \frac{Nu^a}{\Delta T_N} = \frac{Nu^a}{1+\delta T} \sim \delta T^{-1}, \tag{4.5}$$

where the superscript $\varPhi^a$ denotes the achieved values by the simulation under presence of $\Delta T_N \neq 1$.

In addition to the typical definition of the global Nusselt number from (2.12) – considering the fluid domain only – one may also define a CHT Nusselt number Nu_{CHT} which relates the heat current through the entire CHT set-up (including the solid subdomains) to the diffusive heat current through the fluid layer

$$Nu_{CHT}\,(t) := \frac{\langle \boldsymbol{J} \boldsymbol{\cdot} \boldsymbol{e}_z \rangle_V}{\langle \boldsymbol{J}_{dif,f} \boldsymbol{\cdot} \boldsymbol{e}_z \rangle_{V_f}} = \frac{\sum_{\varPhi} \left\langle \boldsymbol{J}_{dif,\varPhi} \boldsymbol{\cdot} \boldsymbol{e}_z \right\rangle_{V_\varPhi} + \left\langle \boldsymbol{u} T_f \boldsymbol{\cdot} \boldsymbol{e}_z \right\rangle_{V_f}}{\langle \boldsymbol{J}_{dif,f} \boldsymbol{\cdot} \boldsymbol{e}_z \rangle_{V_f}} \tag{4.6a}$$

$$= \frac{\langle u_z T \rangle_{V_f}}{\kappa_f \frac{\Delta T_f}{H}} + 1 + \frac{2}{\varGamma_s}\frac{\kappa_s}{\kappa_f}\frac{\Delta T_s}{\Delta T_f} = Nu\,(t) + \frac{2}{\varGamma_s}\frac{\kappa_s}{\kappa_f}\frac{\Delta T_s}{\Delta T_f}, \tag{4.6b}$$

where $\varPhi = \{f, sb, st\}$ and $\Delta T_{s,f}$ are the non-dimensional temperature drops across the solid or fluid, respectively (i.e. $\Delta T_f = \Delta T_N$ and $\Delta T_s = (T_h - T_c - \Delta T_f)/2$). We stress that $Nu_{CHT} \geq Nu$, i.e. it represents the latter plus an additional offset that vanishes for $\kappa_s/\kappa_f \to \infty$ only.

Figure 6 illustrates the overall trends of the size of flow structures and their induced momentum and heat transfer for our two main series of simulations across different κ_s/κ_f. First, see figure 6(*a*), we find that the qualitative impression from figure 5 is clearly supported by $\varLambda_T(\kappa_s/\kappa_f)$. While such a growth of flow structures is in line with our linear stability analysis from § 3, we note that we would expect to see a further but still finite growth of turbulent flow structures for $\kappa_s/\kappa_f \in (10^{-1}, 10^{-1/2})$ if we provided a sufficiently larger numerical domain.

Identifier	t_{ss}	$\varLambda T_N$	$\max(\varDelta_h T)$	$\mathrm{std}(T)$	Nu	Re	$\varLambda_T$	Nu_{CHT}
N4	2000	0.316 ± 0.001	3.04 ± 0.02	0.55 ± 0.00	3.17 ± 0.01	22.82 ± 0.02	29.86 ± 0.00	–
C4N	2250	1.001 ± 0.001	9.66 ± 0.04	1.77 ± 0.00	3.16 ± 0.01	22.79 ± 0.01	29.86 ± 0.00	9.50 ± 0.01
C4a	2250	0.996 ± 0.001	9.12 ± 0.02	1.68 ± 0.00	2.98 ± 0.00	21.85 ± 0.00	29.86 ± 0.00	8.95 ± 0.01
C4b	2000	1.008 ± 0.001	8.16 ± 0.01	1.53 ± 0.00	2.68 ± 0.00	20.20 ± 0.00	29.85 ± 0.00	8.04 ± 0.01
C4c	2000	1.000 ± 0.006	3.74 ± 0.06	0.72 ± 0.01	2.43 ± 0.01	18.61 ± 0.00	25.68 ± 1.10	7.30 ± 0.03
C4d	2000	0.995 ± 0.005	2.12 ± 0.07	0.41 ± 0.01	2.37 ± 0.01	18.21 ± 0.01	15.54 ± 0.78	7.11 ± 0.03
C4e	2000	0.996 ± 0.004	1.19 ± 0.03	0.23 ± 0.00	2.31 ± 0.01	17.85 ± 0.01	9.46 ± 0.29	6.92 ± 0.02
C4f	2000	1.002 ± 0.004	0.64 ± 0.02	0.12 ± 0.00	2.30 ± 0.01	17.81 ± 0.01	6.86 ± 0.17	6.89 ± 0.02
C4g	2000	1.010 ± 0.002	0.34 ± 0.01	0.07 ± 0.00	2.28 ± 0.01	17.67 ± 0.01	5.74 ± 0.11	6.83 ± 0.01
C4D	2000	1.000 ± 0.000	0.00 ± 0.00	0.00 ± 0.00	2.23 ± 0.01	17.36 ± 0.01	4.57 ± 0.10	2.23 ± 0.01
D4	2000	1	–	–	2.24 ± 0.02	17.54 ± 0.01	4.42 ± 0.13	–
N5	2000	0.198 ± 0.001	0.93 ± 0.02	0.16 ± 0.00	5.04 ± 0.03	77.36 ± 0.53	29.83 ± 0.01	–
C5a	2000	1.002 ± 0.004	4.51 ± 0.06	0.78 ± 0.00	4.85 ± 0.05	76.06 ± 0.43	29.83 ± 0.01	14.56 ± 0.07
C5b	2000	1.007 ± 0.004	4.41 ± 0.06	0.77 ± 0.00	4.76 ± 0.05	75.11 ± 0.44	29.83 ± 0.01	14.28 ± 0.06
C5c	2000	1.004 ± 0.003	3.09 ± 0.05	0.55 ± 0.01	4.65 ± 0.04	72.90 ± 0.36	29.43 ± 0.06	13.94 ± 0.05
C5d	2000	1.002 ± 0.002	1.99 ± 0.06	0.33 ± 0.00	4.60 ± 0.04	72.50 ± 0.32	17.52 ± 0.92	13.81 ± 0.04
C5e	2000	1.004 ± 0.002	1.33 ± 0.03	0.23 ± 0.00	4.52 ± 0.04	71.42 ± 0.33	10.52 ± 0.26	13.57 ± 0.04
C5f	2000	1.004 ± 0.001	0.85 ± 0.02	0.15 ± 0.00	4.49 ± 0.04	70.65 ± 0.30	9.23 ± 0.24	13.51 ± 0.04
C5g	2000	1.005 ± 0.001	0.50 ± 0.01	0.09 ± 0.00	4.45 ± 0.03	70.01 ± 0.27	6.86 ± 0.17	13.35 ± 0.03
D5	2000	1	–	–	4.34 ± 0.02	68.60 ± 0.25	4.60 ± 0.09	–
C5cG1	2000	1.003 ± 0.003	1.84 ± 0.05	0.29 ± 0.00	4.69 ± 0.04	72.96 ± 0.34	15.11 ± 0.45	14.06 ± 0.05
C5c	2000	1.004 ± 0.003	3.09 ± 0.05	0.55 ± 0.01	4.65 ± 0.04	72.90 ± 0.36	29.43 ± 0.06	13.94 ± 0.05
C5cG30	2000	0.997 ± 0.003	3.65 ± 0.07	0.63 ± 0.00	4.69 ± 0.04	72.47 ± 0.34	29.71 ± 0.03	14.07 ± 0.05

Table 4. Thermal and global characteristics of the direct numerical simulations listed in table 3. The table contains the analysis time interval in the statistically stationary regime t_{ss} (being part of t_r and situated at its end), the mean temperature difference across the fluid layer ΔT_N, the maximum instantaneous temperature difference $\max(\varDelta_h T)$ as an average of the values from the two solid–fluid interfaces, the instantaneous standard deviation of the temperature field at these interfaces $\mathrm{std}(T)$ (again as average over both interfaces), the global Nusselt number Nu, Reynolds number Re, the pattern size as quantified by the integral length scale $\varLambda_T$, as well as the global CHT Nusselt number Nu_{CHT}. All characteristics are provided as their time-averaged value together with the corresponding standard deviation. Note that the error of Nu_{CHT} has been obtained by calculating the combined uncertainty, regarding Nu and ΔT_N as uncorrelated since the correlation coefficient is unknown. Computing Nu_{CHT}/Nu is in excellent agreement with the theoretical value of $Nu_{CHT}/Nu = 3$ given $\Delta T_N \equiv 1$.

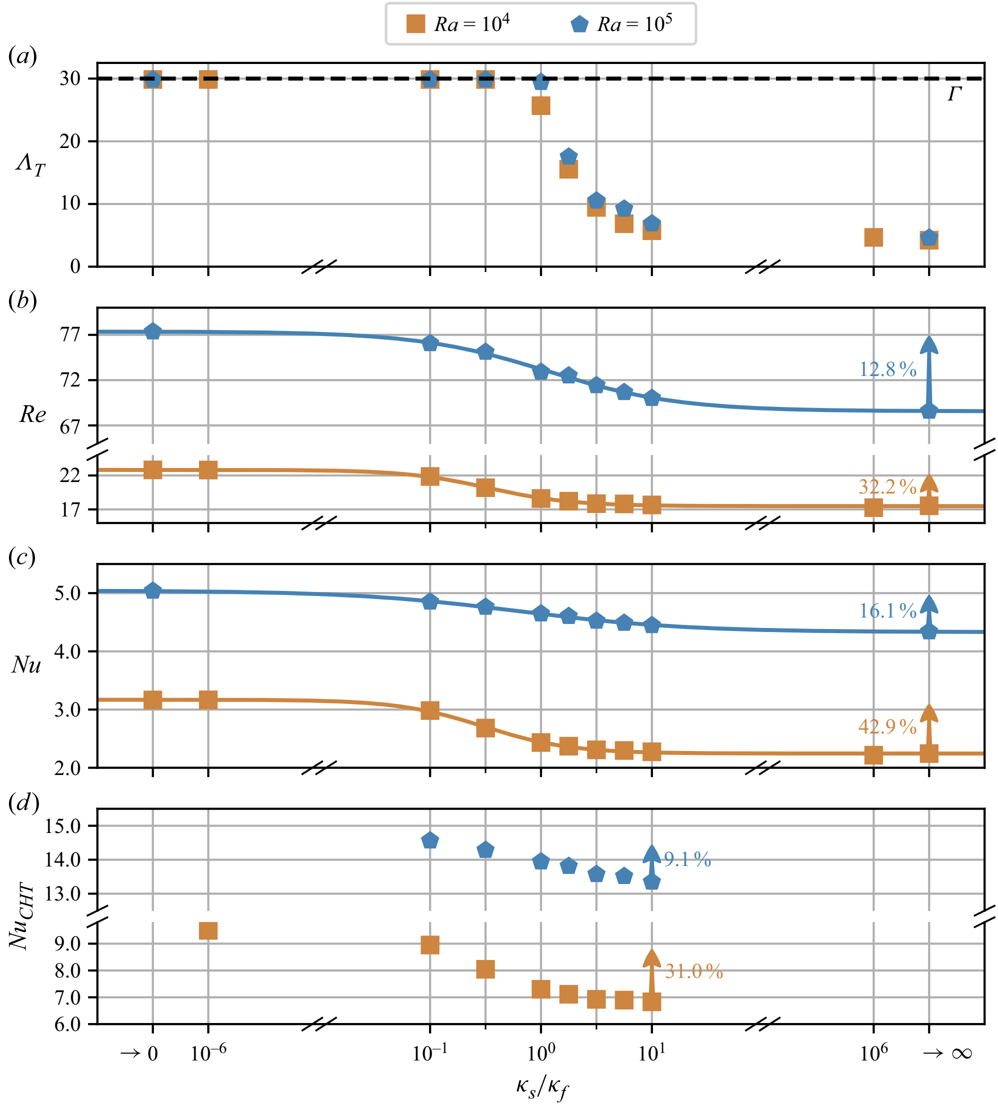

Figure 6. Size of flow structures and their induced transport. The worst solid thermal conductors (relative to the fluid) – and thus the largest flow structures – induce strongest turbulence and the greatest global heat transfer. Solid lines indicate regressions of the data points based on a hyperbolic tangent function with parameters described by table 5 . Here $\varGamma_s = 15$ for all data. Note that, in panel (*d*), $Nu_{CHT}(Ra = 10^4, \kappa_s/\kappa_f = 10^6) = 2.23$ lies beyond the axis limits.

As shown by table 4, larger flow structures – or in other words, smaller κ_s/κ_f – naturally induce stronger thermal heterogeneities at the solid–fluid interfaces. This relaxes the bounds on the temperature field (that is felt by the fluid) and allows thus for a stronger local volumetric forcing in the Navier–Stokes equation (2.2). As a result, we find an increased global transfer of momentum as shown by $Re(\kappa_s/\kappa_f)$ in figure 6(*b*). Consequently and similarly, also the global heat transfer across the fluid layer is enhanced as measured by $Nu(\kappa_s/\kappa_f)$ in figure 6(*c*). These trends are in line with previous results by Vieweg (2023) for the extreme Neumann and Dirichlet cases. In addition, see figure 6(*d*), $Nu_{CHT}(\kappa_s/\kappa_f)$ offers trends similar to $Nu(\kappa_s/\kappa_f)$.

f	Ra	a	b	c	d	R^2
Nu	10^4	−0.463	0.558	0.660	2.708	0.9985
Nu	10^5	−0.357	0.286	0.152	4.687	0.9982
Re	10^4	−2.673	0.578	0.630	20.158	0.9981
Re	10^5	−4.402	0.369	−0.055	72.969	0.9973

Table 5. Regression parameters for Nu and Re. A tanh-fit of the form $f(\kappa_s/\kappa_f, Ra) = a \tanh[b \ln(\kappa_s/\kappa_f) + c] + d$ is applied to the values in figure 6. Here R^2 is the coefficient of determination (Wright 1921) and underlines the quality of these fits.

Starting from the Dirichlet- and moving towards the Neumann case, we find that both Re and Nu experience substantial increases of up to 32 % and 43 %, respectively. Albeit these relative changes decrease with increasing Ra due to the increased turbulent mixing, the absolute change of Re seems still to increase. This underlines that thermal boundary conditions may even affect scaling laws such as $Nu \sim Ra^{\gamma}$ (Plumley & Julien 2019; Vieweg 2023) in certain ranges. In more detail, the trends in global heat transfer across the fluid layer of our three-dimensional CHT simulations in a square $\varGamma = 30$ domain align qualitatively with the ones of Johnston & Doering (2009), the latter of which compared the Dirichlet and Neumann cases for $\varGamma = 2$ at $Ra \leqslant 10^{10}$ in a two-dimensional domain and found that Nu is increased in the Neumann case for $Ra \lesssim 10^6$. In contrast, the impact of the thermal boundary conditions vanished for $Ra > 10^6$. The same trend was observed by Vieweg (2023) for three-dimensional domains of square $\varGamma = 60$ at $Ra \lesssim 10^7$ and by Verzicco & Sreenivasan (2008) in a cylinder of $\varGamma = 1/2$ at $Ra > 10^9$. Albeit this evidence may lead one to suspect that the impact of κ_s/κ_f on Nu and Re vanishes for $Ra \gg 10^5$ due to increased turbulent mixing, further studies at higher Ra are required to prove it.

In analogy to § 3, we apply hyperbolic tangent fits to our numerical data. While the resulting fits are included in figure 6, their underlying parameters are provided in table 5 and allow us to estimate expected values of Re and Nu given $Pr = 1$ and $Ra = \{10^4, 10^5\}$ under different κ_s/κ_f. Reminiscent of § 3, we observe again an asymmetric behaviour with the inflection point being skewed towards $\kappa_s/\kappa_f < 10^0$.

5. Boundary layer analysis

Albeit the global heat and momentum transport through the fluid layer have been quantified in § 4.3, detailed knowledge of both its thermal and viscous boundary layers is essential, too. On the one hand, the thermal boundary layers account for the majority of the temperature drop across the fluid layer (Scheel *et al.* 2013; Vieweg *et al.* 2021) and thus induce the essential destabilisation of the latter. On the other hand, the viscous boundary layers are highly dissipative regions (Scheel *et al.* 2013; Vieweg *et al.* 2021) that slow down fluid motions towards the walls and insinuate the strong turbulence present in the adjacent bulk.

While the thermal boundary layer thickness is traditionally defined based on the mean (conductive) heat transfer at the top and bottom boundaries (Chillà & Schumacher 2012)

$$\delta_T = \frac{1}{2\,Nu}, \tag{5.1}$$

there is no equivalent transfer of momentum at these planes into the fluid. Instead, the viscous boundary layer is generated by randomly oriented patches of shear flow and usually lacks a mean flow (Samuel *et al.* 2024). This structure suggests an alternative measure of the boundary layer thickness based on the full and horizontal velocity fluctuation profiles

$$u_{rms}\,(z) = \sqrt{\left\langle u_x^2 + u_y^2 + u_z^2 \right\rangle_{A,t}} \quad \text{and} \quad u_{rms}^h\,(z) = \sqrt{\left\langle u_x^2 + u_y^2 \right\rangle_{A,t}} \tag{5.2}$$

where the maxima mark the viscous fluctuation thicknesses $\delta_{u,rms}$ and $\delta_{u,rms}^h$, respectively. Equivalently, a similar definition for the thermal fluctuation thickness $\delta_{\Theta,rms}$ is given by the maximum of the temperature fluctuation profile

$$\Theta_{rms}\,(z) = \sqrt{\left\langle \Theta^2 \right\rangle_{A,t}} \tag{5.3}$$

which has been found to strongly correlate with δ_T (Long *et al.* 2020). Note the difference between this profile of Θ_{rms} and its global quantity defined in (4.2).

We prepare this analysis of thermal and viscous boundary layers by increasing the spatial resolution of our simulations: after t_r (see table 3), we change the vertical number of spectral elements within the fluid layer from four to six – leading to at least 14 grid points within a boundary layer – and relax the flow onto this new grid for $50\tau_f$ before analysing the subsequent $100\tau_f$. Moreover, we rescale the temperature field for the following postprocessing based on the original ΔT_N (Vieweg 2023, 2024*a*) for improved comparability between the Neumann and remaining cases.

Figure 7 illustrates the mean temperature profiles across our different κ_s/κ_f for $Ra = 10^4$ in figure 7(*a,b*) and $Ra = 10^5$ in figure 7(*d,e*). Bridging the gap between idealised thermal boundary conditions reported in Pandey *et al.* (2022) and Vieweg (2023, 2024*a*), our CHT set-up exhibits at this intermediate $Pr = 1$ an increased tendency for a manifestation of a (weak) stable stratification in the bulk of the fluid layer when decreasing κ_s/κ_f. This stratification is the result of weakly mixing thermal plumes that detach and shoot deep into or even through the bulk (Vieweg 2024*a*). This might be supported by an increased size and thus large-scale organisation of the flow structures. As the (classical) thermal boundary layer thickness δ_T is directly linked to Nu, we find that δ_T decreases with decreasing κ_s/κ_f. As Nu tends to become more independent of κ_s/κ_f for larger Ra (see again figure 6), δ_T converges as well. As an alternative to this classical measure, figure 7(*c,f*) visualise the thermal fluctuation thicknesses $\delta_{\Theta,rms}$. Given natural thermal boundary conditions that are more similar to the Dirichlet case, δ_T and $\delta_{\Theta,rms}$ converge as Ra is increased (Samuel *et al.* 2024). However, for conditions more similar to the Neumann case with smaller values of κ_s/κ_f, the definition of $\delta_{\Theta,rms}$ loses significance as worse solid thermal conductors imply quicker relaxations of thermal perturbations in the fluid and thus a shift of these peaks of variance closer to (or even into) the solids.

Figure 8 moves the focus of the boundary layer analysis to the velocity field. As shown across the entire fluid domain in figure 8(*a,d*), we observe pronounced peaks in the fluctuation profiles especially for smaller κ_s/κ_f, i.e. for more pronounced large-scale organisations of the flow. Especially figure 8(*a*) indicates the presence of dominant, horizontally extended convection rolls that offer strong horizontal velocities, see also figure 8(*b,c*). Interestingly, despite the very different amplitudes of these profiles across κ_s/κ_f, the viscous boundary layer thickness is very similar and varies only weakly with Ra (and thus Re). In other words, the viscous boundary layer thickness varies less with both κ_s/κ_f and Ra than the thermal one. As a result, the ratio $\delta_{u,rms}/\delta_{\Theta,rms}$ tends to increase for larger Ra (Samuel *et al.* 2024). However, our data suggests that it is not solely Re that governs the thickness of the viscous boundary layer: for fixed Ra, our Re is larger for smaller

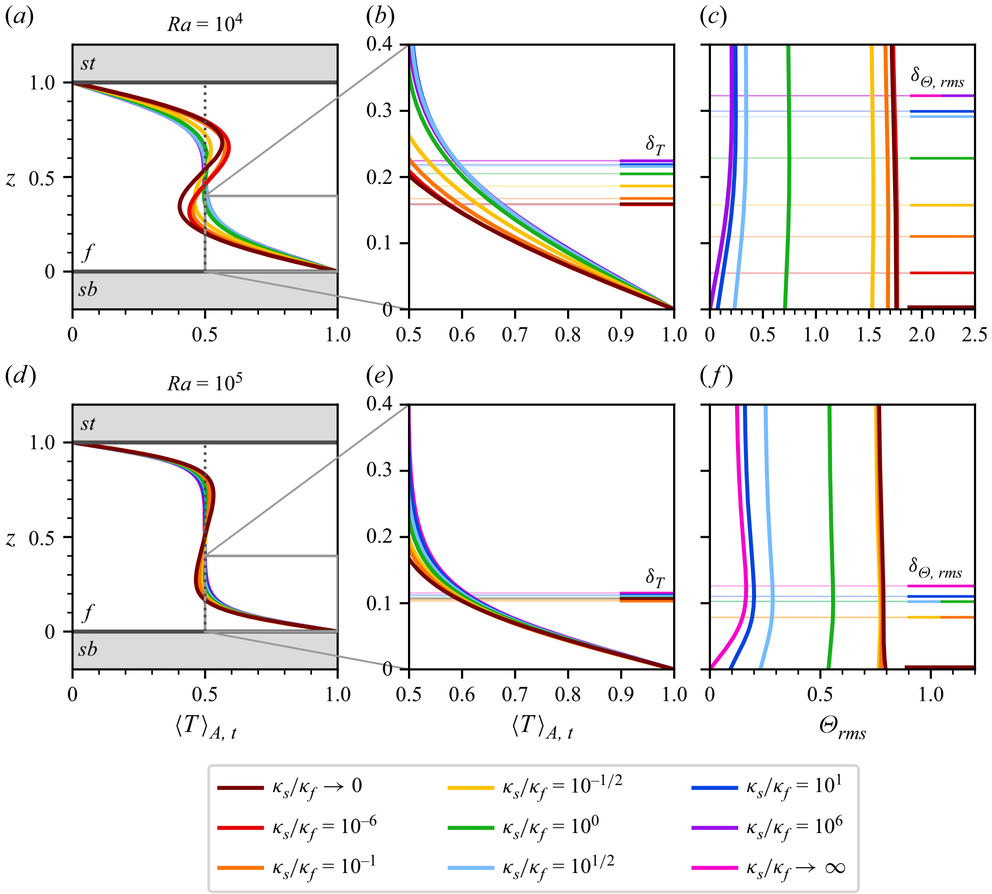

Figure 7. Thermal boundary layer analysis. Although a glimpse at (*a,d*) the entire vertical profiles shows only little variation of them with κ_s/κ_f, a closer look at the bottom region for both the planar (*b,e*) average and (*c,f*) variation reveals a more pronounced dependence of appropriately defined boundary layer thicknesses δ_T and $\delta_{\Theta,rms}$ (as indicated by the horizontal lines). Note that we exploit the rescaled temperature field for this analysis and $\Gamma_s = 15$ for all data.

κ_s/κ_f even though both $\delta_{u,rms}$ and $\delta^h_{u,rms}$ exhibit the opposite trend. This suggests that long-living large-scale flow structures play a crucial role even for viscous boundary layers.

6. The impact of the plate thickness

6.1. *Choice of the vertical aspect ratio* Γ_s

In all our simulations discussed so far, a vertical aspect ratio of $\Gamma_s = 15$ has been used. This deliberate choice is based on a diffusion time argument: temperature differences are supposed to relax more quickly in the horizontal than in vertical direction,

$$\tau_{\kappa,s,v} \overset{!}{\geqslant} \tau_{\kappa,s,h} \quad \text{with} \quad \tau_\kappa = \frac{L_{ch}^2}{\kappa}, \tag{6.1}$$

promoting a weak to negligible footprint of the applied thermal boundary conditions on the solid–fluid interfaces. Given our laterally periodic domain, the largest structure satisfying this condition has a horizontal extend of $L_{ch,h} = L/2 = \Gamma H/2$. Hence, condition (6.1) turns into

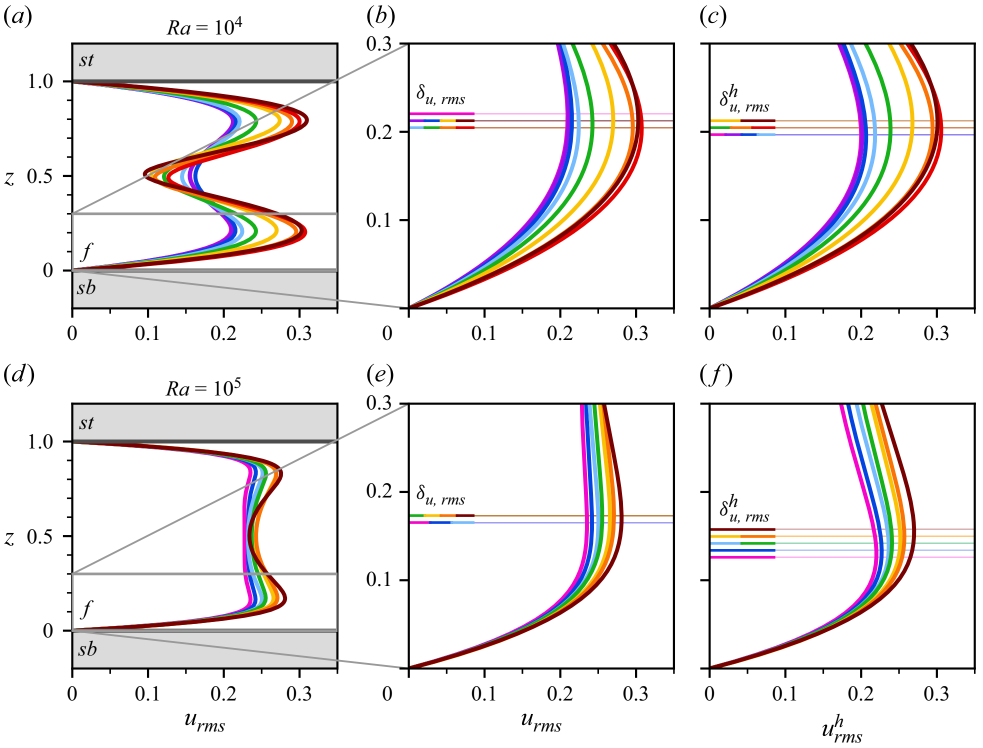

Figure 8. Viscous boundary layer analysis. While in (*a,d*) the entire vertical profiles highlight the presence of dominant horizontally extended flow structures in particular for smaller κ_s/κ_f and Ra, these profiles' variation allows to derive and contrast appropriately defined boundary layer thicknesses $\delta_{u,rms}$ (as indicated by the horizontal lines) for both the full as well as only the horizontal velocity field. Note that $\Gamma_s = 15$ for all data and the colour encoding coincides with figure 7.

$$\frac{H_s^2}{\kappa_s} \overset{!}{\geqslant} \frac{L^2/4}{\kappa_s} = \frac{\Gamma^2 H^2}{4\kappa_s} \Leftrightarrow \Gamma_s \geq \frac{\Gamma}{2} \tag{6.2}$$

and a domain of $\Gamma = 30$ should offer (at least) $\Gamma_s = 15$.

Figure 9 scrutinises our condition (6.2) by plotting and contrasting vertical profiles of the standard deviation in the temperature field $\mathrm{std}(T)$ across all κ_s/κ_f in figure 9(*a*). We find that the propagation of thermal inhomogeneities into the solid plates is asymmetric with respect to κ_s/κ_f. Interestingly, thermal perturbations relax most slowly in case of $\kappa_s/\kappa_f = 10^0$ despite its weaker thermal inhomogeneities at the solid–fluid interface compared with $\kappa_s/\kappa_f = \left\{10^{-1}, 10^{-1/2}\right\}$ (see also again table 4).

In order to probe the impact of our applied thermal boundary condition at $z = 1 + \Gamma_s$ (see (2.9)), we proceed by varying Γ_s given a fixed $\kappa_s/\kappa_f = 10^0$. Figure 9(*b*) contrasts two additional simulations of $\Gamma_s = \{1, 30\}$ with the previous case. On the one hand, we find that thin plates of $\Gamma_s = 1$ result in significant decreases of the thermal inhomogeneities and size of the resulting flow structures compared with $\Gamma_s = 15$, see also again table 4. This suggests that temperature differences in the horizontal direction are not sufficiently relaxed and that the underlying thermal boundary conditions leave a considerable footprint on the solid–fluid interfaces. On the other hand, even thicker plates of $\Gamma_s = 30$ do not seem to provide a significant benefit. Despite somewhat larger inhomogeneities at the solid–fluid interfaces, the vertical profile underlines that the relaxation of thermal inhomogeneity is barely altered despite a doubling of the plate thickness. Hence, we

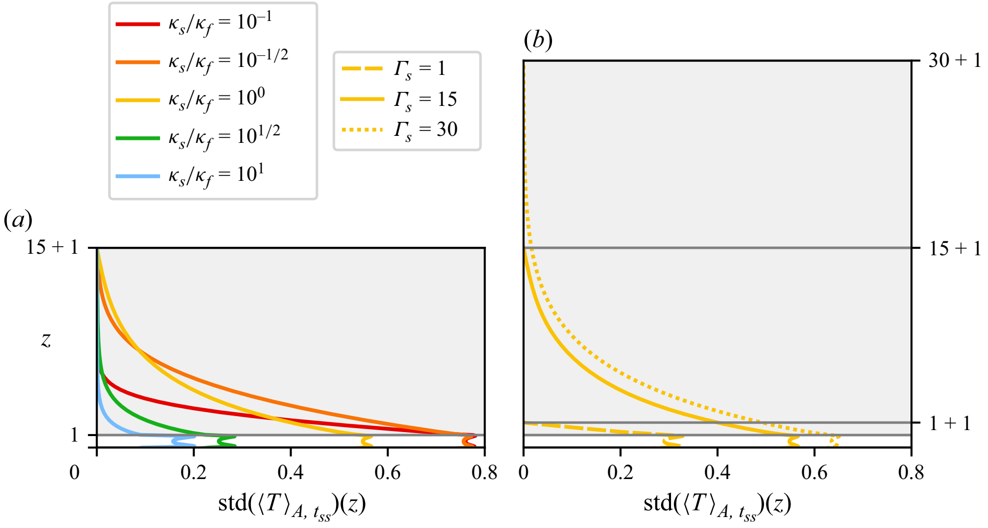

Figure 9. Relaxation of turbulent flow-induced thermal perturbations across the solid plates. (*a*) Given $\Gamma_s = 15$ (at $Ra = 10^5$), the relaxation is slowest close to a unity ratio $\kappa_s/\kappa_f = 10^0$. Even for this critical case, (*b*) the situation has mostly converged to that with plates of even twice the thickness. In contrast, thinner plates with $\Gamma_s = 1$ impact the temperature field at the solid–fluid interfaces strongly. The situation is symmetric for $-\Gamma_s \leq z \leq 0$.

conclude that the choice of $\Gamma_s = 15$ based on condition (6.2) for our main production simulations has been appropriate.

6.2. *Linear stability analysis for different plate thicknesses Γ_s*

Similar to the turbulent flow at $Ra \gg Ra_c$, we expect the onset of convection to be affected by the thickness of the solid plates Γ_s. As shown in Appendix A, we extend the work of Hurle *et al.* (1967) (who considered $\Gamma_s \to \infty$) by respecting the plate thickness via the $-\lambda_f/\lambda_s \tanh(k\Gamma_s)$ term in the solution of the linear stability of the system (see (3.1)).

Figure 10 compares various neutral stability curves given constant λ_s/λ_f in different panels. On the one hand, we find that the curves (across the different panels) converge for infinitely small vertical aspect ratios $\Gamma_s \to 0$ – independently of λ_s/λ_f – towards the classical Dirichlet case (i.e. the violet curves are all the same). This case, making any plates obsolete, is certainly influenced by our applied Dirichlet-type boundary conditions at the very top and bottom. On the other hand, we observe that the curves (in each panel) converge for large vertical aspect ratios $\Gamma_s \gg 1$ independently of λ_s/λ_f. In other words, there is practically no difference between $\Gamma_s = 15$ and $\Gamma_s \to \infty$. This substantiates our choice of $\Gamma_s = 15$ in § 6.1. Additionally, we find that the neutral stability curves converge for $\lambda_s/\lambda_f \to \{0, \infty\}$ as long as $\Gamma_s > 0$ and sufficiently large (e.g. $\Gamma_s = 0.1$). Only a zoom towards $k \approx 0$, see figure 10(*d*), indicates the gradual convergence of the critical wavenumber for the Neumann case as one of these two idealised thermal boundary conditions. For such small, yet positive λ_s/λ_f, the solid plates conduct heat way worse than the fluid, and so even very thin plates of $\Gamma_s = 0.1$ effectively act insulating. This may have important implications for any coating of a wall in laboratory convection set-ups (Schindler *et al.* 2022, 2023; Wondrak *et al.* 2023).

The situation becomes significantly more complex once no limit of either Γ_s or λ_s/λ_f is considered. Contrasting figure 10(*b,c,e,f*), a certain asymmetry around $\lambda_s/\lambda_f = 10^0$ can (once again) be noticed. While the neutral stability curves almost coincide for $\lambda_s/\lambda_f = 10^1$

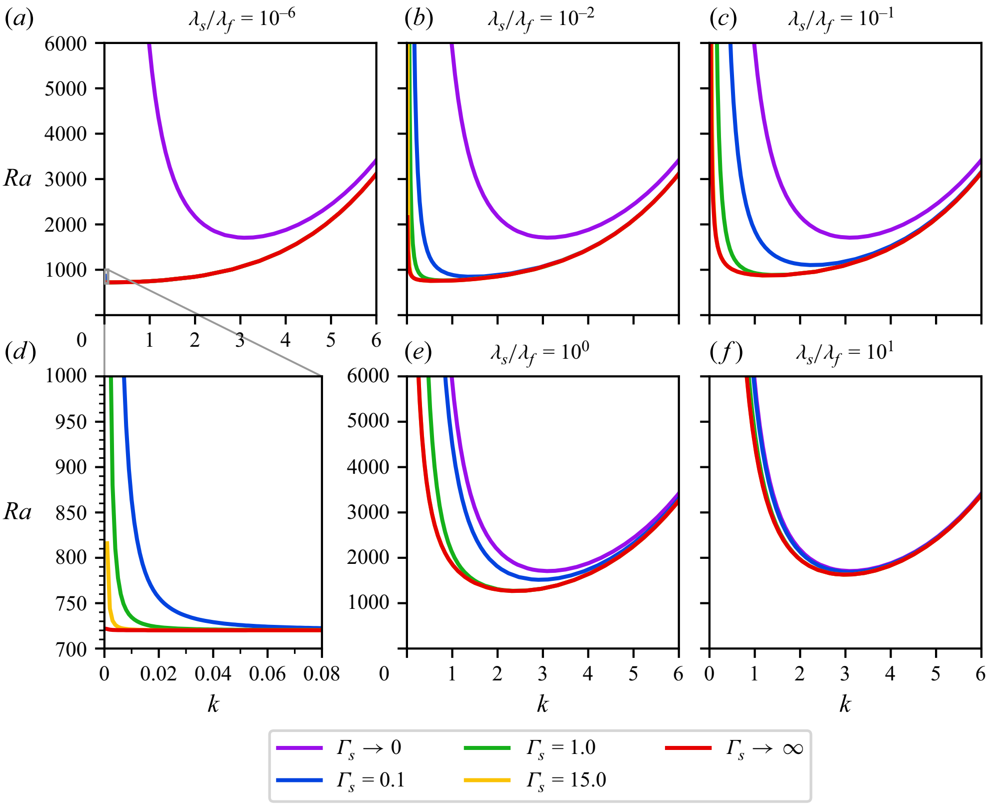

Figure 10. Neutral stability across varying Γ_s. While vertically infinitely extended plates are already resembled at $\Gamma_s \gg 1$, thinner plates $\Gamma_s \lesssim 1$ impact the system significantly and stabilise the layer successively. Worse solid thermal conductors (relative to the fluid) are more strongly affected by this stabilisation; contrast therefore in particular panels (*c*,*f*) which are symmetrically spaced around $\lambda_s/\lambda_f = 10^0$.

in figure 10(*f*), there is a significant spread for $\lambda_s/\lambda_f = 10^{-1}$ in figure 10(*c*). This begs the following question: Which ratio of thermal conductivities is most sensitive to a variation of Γ_s?

In an attempt to quantify the divergence of the neutral stability curves, we measure the differences in Ra_c and k_c between the cases of $\Gamma_s = 0.1$ and $\Gamma_s \to \infty$ via

$$\Delta Ra_c\left(\frac{\lambda_s}{\lambda_f}\right) = Ra_c\left(\frac{\lambda_s}{\lambda_f},\, \Gamma_s = 0.1\right) - Ra_c\left(\frac{\lambda_s}{\lambda_f},\, \Gamma_s \to \infty\right), \tag{6.3}$$

$$\Delta k_c\left(\frac{\lambda_s}{\lambda_f}\right) = k_c\left(Ra_c\left(\frac{\lambda_s}{\lambda_f},\, \Gamma_s = 0.1\right)\right) - k_c\left(Ra_c\left(\frac{\lambda_s}{\lambda_f},\, \Gamma_s \to \infty\right)\right). \tag{6.4}$$

Figure 11 illustrates these results. Note that while $\Delta Ra_c > 0$ implies a stabilisation of the convection layer when decreasing the thickness of the solid plates, $\Delta k_c > 0$ indicates a decrease in the size of critical flow structures. Moreover, we find that both ΔRa_c and Δk_c offer pronounced peaks around $\lambda_s/\lambda_f \approx 10^{-0.5}$ and $\lambda_s/\lambda_f \approx 10^{-1}$, respectively. Supported by the general asymmetry of these curves, this analysis underlines the complex ramifications an interplay between the solid and fluid domain can exhibit.

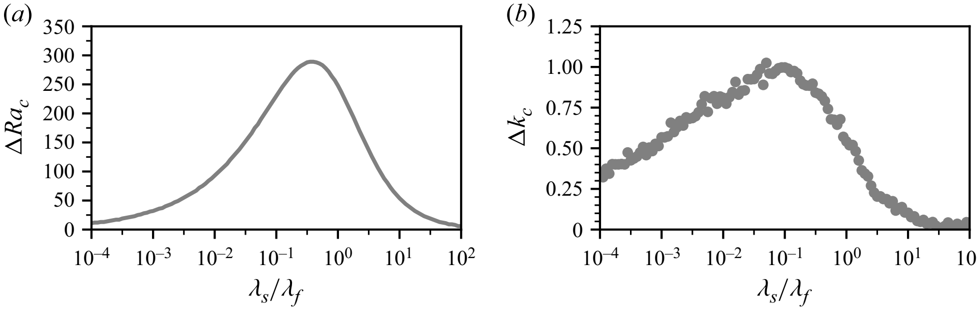

Figure 11. Sensitivity of neutral stability on plate thickness for varying λ_s/λ_f. The differences in Ra_c (*a*) and corresponding k_c (*b*) are shown when moving from infinitely thick ($\Gamma_s \to \infty$) towards very thin plates ($\Gamma_s = 0.1$). Decreasing Γ_s thus stabilises the layer successively, with the strongest impact near $\lambda_s/\lambda_f \approx 10^{-1/2}$, not just shifting the onset of convection, but also reducing the initial pattern size at this point.

7. Discussion and perspective

Long-living large-scale flow structures are crucial for an understanding and prediction of convection flows such as in the Earth's atmosphere. Previous studies of horizontally extended Rayleigh–Bénard convection focussed on idealised thermal boundary conditions such as constant temperatures (the so-called Dirichlet case) or a constant heat flux (Neumann case) (Pandey *et al.* 2018; Vieweg *et al.* 2021; Vieweg 2023). However, these conditions reduce the problem to the fluid layer only and thus represent rather idealised cases. In contrast, any natural convection flow is confined by some adjacent matter. Using a coupled or CHT set-up, this study includes two identical fluid-confining solid plates at the bottom and the top of the fluid layer. The ratio of thermal diffusivities κ_s/κ_f between the solids and the fluid represents the key control parameter characterising the (to the perspective of the fluid) resulting thermal boundary conditions. The inclusion of solid subdomains allows us to resemble the Neumann case via $\kappa_s/\kappa_f \to 0$ and the Dirichlet case via $\kappa_s/\kappa_f \to \infty$, see Appendix B. Varying κ_s/κ_f across a broad range, this study bridges the gap in between by introducing natural thermal boundary conditions.

Given a Prandtl number $Pr = 1$, (horizontal) aspect ratio $\Gamma = 30$ and thickness of the solid plates $\Gamma_s = 15$, we have conducted direct numerical simulations subject to varying κ_s/κ_f for $Ra = \left\{10^4, 10^5\right\}$ under no-slip boundary conditions at the solid–fluid interfaces and periodic boundary conditions concerning the lateral extent of the domain of square horizontal cross-section. As shown in figure 4, such a coupled system allows for highly complex dynamics of both T and $\partial T/\partial z$ at the various (partly solid–fluid) interfaces based on the manifesting fluid flow.

Varying κ_s/κ_f from $\kappa_s/\kappa_f \gg 10^0$ towards $\kappa_s/\kappa_f \ll 10^0$, we found that both structural as well as statistical properties of the flow undergo significant changes: the long-living large-scale flow structures grow, and both their induced momentum and heat transfer are (asymmetrically with respect to κ_s/κ_f) increased by up to 43 %. The increase of these measures can be explained by stronger thermal inhomogeneities – the footprints of these flow structures – at the solid–fluid interfaces and align with recent results for idealised thermal boundary conditions (Vieweg *et al.* 2021; Vieweg 2023) or strongly asymmetric CHT set-ups (Vieweg *et al.* 2025). We observe a gradual transition from turbulent superstructures towards supergranules, underlining the importance of the umbrella term of long-living large-scale flow structures (Vieweg 2023).

A linear stability analysis of our CHT set-up confirms both the growth of flow structures as well as an increased heat transfer for smaller values of λ_s/λ_f. In other words, we observe a monotonic shift of both the critical Rayleigh number Ra_c and critical wavenumber k_c when varying λ_s/λ_f between its limits. This implies a change in the supercriticality Ra/Ra_c given a fixed $Ra > Ra_c$ and affects thus the induced heat transfer.

We have extended the previous work by Hurle *et al.* (1967) with respect to two important aspects: first, we provided simple relations or regressions for $k_c(\lambda_s/\lambda_f)$, $Ra_c(\lambda_s/\lambda_f)$, and $Ra_c(k_c)$ – see again table 2. This hopefully improves the accessibility of our results. Second, we investigated the impact of a finite thickness of the solid plates in § 6.2, allowing us to understand the convergence of the system for the limits $\left\{\varGamma_s, \lambda_s/\lambda_f\right\} \rightarrow \{0, \infty\}$ and find its point of largest susceptibility to a change in the plate thickness (as quantified by ΔRa_c) at $\lambda_s/\lambda_f \approx 10^{-1/2}$.

This effect of a varying plate thickness $\varGamma_s$ was additionally studied numerically. We found that $\varGamma_s \lesssim 1$ tends to stamp the external thermal boundary condition onto the internal solid–fluid interface, whereas our chosen $\varGamma_s = 15 \gg 1$ represents a fair approximation of $\varGamma_s \rightarrow \infty$. We note at this point that the computational cost of one CHT simulation involving $\varGamma_s = 15$ increases the required wallclock solution time by a factor of roughly 8 compared with a simulation without solid plates (for the same number of non-dimensional time units τ_f). Both this numerical investigation of varying $\varGamma_s$ as well as the corresponding investigation of the linear stability have important implications for the design of laboratory experiments (Foroozani *et al.* 2021; Moller, Resagk & Cierpka 2021; Moller 2022; Wondrak *et al.* 2023; Vieweg *et al.* 2025).

An additional analysis of both the thermal and viscous boundary layers confirmed an increasing ratio between these thicknesses, $\delta_{u,rms}/\delta_{\Theta,rms}$, for increasing Ra (Samuel *et al.* 2024), even though we considered two different Rayleigh numbers only. However, our data suggests that long-living large-scale flow structures play an important role in the formation of $\delta_{u,rms}$, so that the latter is not solely governed by Re.

In nature, thermal convection flows offer typical ratios of thermal diffusivities in the range of $\kappa_s/\kappa_f \approx [10^{-3}, 10^{-1}]$ (see again table 1). Such values are not only clearly between the typically studied cases of $\kappa_s/\kappa_f \rightarrow 0$ and $\kappa_s/\kappa_f \rightarrow \infty$, but also shifted towards the only more recently investigated Neumann case (Vieweg *et al.* 2021, 2022, 2024; Vieweg 2024*a*). Albeit we have covered corresponding values of κ_s/κ_f, natural flows exhibit far greater Ra and potentially smaller Pr as well as additional mechanisms like rotation (Schumacher & Sreenivasan 2020; Vieweg *et al.* 2022). This present study can be seen as an important, yet early step towards understanding these more demanding and sophisticated geophysical and astrophysical systems. Our recent work (Vieweg *et al.* 2025) already started investigating asymmetric top and bottom plates and thermal boundary conditions as present in scientific engineering applications. Together with additional rotation around the vertical axis (Vieweg *et al.* 2022), this may represent an interesting potential path for future extensions relevant to core–core–mantle or core–ocean–ice configurations found on Earth or icy moons, respectively. Given this last discussion, the present work can define a starting point for further investigations on non-ideal boundary condition effects only.

Acknowledgements. P.P.V. gratefully acknowledges the support of Pembroke College, Cambridge, through a postdoctoral research associateship.

Funding. P.P.V. is funded by the Deutsche Forschungsgemeinschaft (DFG, German Research Foundation) within Walter Benjamin Programme 532721742. M.E. is funded by the Carl Zeiss Foundation with project number P2022-08-006. The authors gratefully acknowledge the Gauss Centre for Supercomuting e.V. (www.gauss-centre.eu) for funding this work by providing computing resources through the John von Neumann Institute for Computing (NIC) on the GCS supercomputer JUWELS at Jülich Supercomputing Center (JSC) within project nonbou. They further acknowledge the computing centre of the Technische Universität Ilmenau for providing access to, as well as computing and storage resources on its compute cluster MaPaCC24.

Declaration of interests. The authors report no conflict of interest.

Author contributions. P.P.V. and J.S. designed the study. M.E. performed the numerical simulations and processed the generated data. All authors contributed equally in discussing the data and writing the paper.

Appendix A. Linear stability analysis for the coupled system

A.1. *Key idea of the linear stability analysis*

The aim of the linear stability analysis is to find the point of the onset of convection with the fluid being initially at rest. The system is considered stable if perturbations, induced as infinitesimally small fluctuations in the form of planar waves, decay. Vice versa, it is unstable if such perturbations grow over time. The analysis is termed linear since one linearises the governing equations with respect to the (infinitesimally small) perturbations.

As it will turn out, the point of the onset of convection is determined by the critical Rayleigh number Ra_c and is caused by the normal mode of the critical wavenumber k_c. In order to transition from a linearly stable to a linearly unstable state, the system must pass the so-called marginal state – which is exactly the one defining these critical numbers (Chandrasekhar 1981).

In the following, the linear stability analysis for the CHT case will be performed. This will yield not only the neutral stability curves for different thermal conductivity ratios λ_s/λ_f, the former of which represent the marginal states via $Ra(k)$, but also the critical Rayleigh numbers Ra_c and wavenumbers k_c as given by their global minimum.

A.2. *Governing equations and boundary conditions*

We consider the same set-up as shown in figure 1(*b*). As long as $Ra < Ra_c$, we are in a non-convective regime and the fluid is at rest. As mentioned in § 2.2 and laid out in more detail in Vieweg *et al.* (2025), in both the solids and the fluid the temperature profile will be linear. For further analysis it will be beneficial to use the temperature deviation $\Theta(\boldsymbol{x}, t)$. It is the deviation of the actual temperature profile from the linear one (which is present in a non-convective case) for both the solids and the fluid

$$\Theta_\Phi(\boldsymbol{x}, t) = T_\Phi(\boldsymbol{x}, t) - T_{lin,\Phi}(z), \quad \text{with} \quad \Phi = \{f, sb, st\}. \tag{A1}$$

For this analysis, we use the governing equations (2.1)–(2.4) based on a different non-dimensionalisation. Instead of the free-fall-inertia-balance (favourable for large Re), we consider a scaling based on the viscous diffusion time scale $\tau_\nu = H^2/\nu$ leading to

$$\tilde{\nabla} \cdot \tilde{\boldsymbol{u}} = 0, \tag{A2}$$

$$\frac{\partial \tilde{\boldsymbol{u}}}{\partial t} + (\tilde{\boldsymbol{u}} \cdot \tilde{\nabla})\tilde{\boldsymbol{u}} = -\tilde{\nabla}\tilde{p} + \tilde{\nabla}^2\tilde{\boldsymbol{u}} + Ra\tilde{\Theta}\boldsymbol{e}_z, \tag{A3}$$

$$Pr\frac{\partial \tilde{\Theta}_f}{\partial \tilde{t}} + Pr(\tilde{\boldsymbol{u}} \cdot \tilde{\nabla})\tilde{\Theta}_f = \tilde{\nabla}^2\tilde{\Theta}_f + \tilde{u}_z, \tag{A4}$$

$$Pr\frac{\kappa_f}{\kappa_s}\frac{\partial \tilde{\Theta}_s}{\partial \tilde{t}} = \tilde{\nabla}^2\tilde{\Theta}_s. \tag{A5}$$

Equations (A2)–(A5) are completed by corresponding boundary conditions. In our set-up, mechanical no-slip boundary conditions are applied at both interfaces. Due to the present symmetry in our domain, we place the origin of the z-coordinate at the midplane of the fluid layer. Together with the continuity equation (A2), this results in

$$\tilde{\boldsymbol{u}}\ (\tilde{z} = \pm 1/2) = 0, \tag{A6}$$

$$\left.\frac{\partial \tilde{u}_z}{\partial \tilde{z}}\right|_{\tilde{z}=\pm 1/2} = 0. \tag{A7}$$

As the subdomains are coupled at the solid–fluid interfaces, both the temperatures and heat fluxes must match there which leads to

$$\tilde{\Theta}_f\ (\tilde{z} = 1/2) = \tilde{\Theta}_{st}\ (\tilde{z} = 1/2)\,, \tag{A8}$$

$$\tilde{\Theta}_f\ (\tilde{z} = -1/2) = \tilde{\Theta}_{sb}\ (\tilde{z} = -1/2)\,, \tag{A9}$$

$$\left.\frac{\partial \tilde{\Theta}_f}{\partial \tilde{z}}\right|_{\tilde{z}=1/2} = \frac{\lambda_{st}}{\lambda_f}\left.\frac{\partial \tilde{\Theta}_{st}}{\partial \tilde{z}}\right|_{\tilde{z}=1/2}, \tag{A10}$$

$$\left.\frac{\partial \tilde{\Theta}_f}{\partial \tilde{z}}\right|_{\tilde{z}=-1/2} = \frac{\lambda_{sb}}{\lambda_f}\left.\frac{\partial \tilde{\Theta}_{sb}}{\partial \tilde{z}}\right|_{\tilde{z}=-1/2}. \tag{A11}$$

We shall omit the tildes in the following for better readability.

A.3. *Perturbation equations*

Next, we apply infinitesimally small perturbations to the system by using a linear combination of basic perturbations. This forms a full set and allows us to extract the one at which instability first occurs. All variables will be subject to the perturbation ϕ' with $\varepsilon \ll 1$ as a perturbation parameter, such that the base state $\bar{\phi}$ is disturbed via

$$\phi = \bar{\phi} + \varepsilon\phi' \quad \text{for} \quad \phi = \{\boldsymbol{u}, p, \Theta\}. \tag{A12}$$

Applying the curl to (A3) twice allows us to drop the pressure term. At this point, the infinitesimally small perturbations are applied to all variables. Keeping in mind that the fluid is at rest and the temperature deviation is absent for the base state, implying

$$\bar{\boldsymbol{u}} = 0 \quad \text{and} \quad \bar{\Theta} = 0, \tag{A13}$$

as well as dividing by $\varepsilon \neq 0$ and dropping all terms of $O(\varepsilon^2)$ since $\varepsilon \ll 1$ (i.e. $\varepsilon^2 \lll 1$) yields the linearised equations

$$\nabla \boldsymbol{\cdot} \boldsymbol{u}' = 0, \tag{A14}$$

$$\frac{\partial(\nabla^2 \boldsymbol{u}')}{\partial t} = \nabla^4 \boldsymbol{u}' + Ra\left(\nabla^2 \Theta'_f - \nabla\frac{\partial \Theta'_f}{\partial z}\right), \tag{A15}$$

$$\frac{\partial \Theta'_f}{\partial t} = \nabla^2 \Theta'_f + u'_z, \tag{A16}$$

$$Pr\frac{\kappa_f}{\kappa_s}\frac{\partial \Theta'_s}{\partial t} = \nabla^2 \Theta'_s. \tag{A17}$$

In a next step, a normal mode ansatz is applied: we assume an infinitely extended domain in the horizontal directions (in line with our laterally periodic boundary conditions) and use the linear equations (A14)–(A17) to superpose plane waves or normal modes which form a complete set of basis functions. These key features allow for linear superposition in the first place and later for an extraction of the wave at which instability occurs first. Such plane waves are given by

$$\phi' = \hat{\phi}'\,(z)\, e^{\mathrm{i}(k_x x + k_y y) + \sigma t}, \tag{A18}$$

where $k_{x,y}$ are the wavenumbers in x and y directions, defining the horizontal wavenumber

$$k_h = k = \sqrt{k_x^2 + k_y^2}. \tag{A19}$$

Here $\sigma \in \mathbb{C}$ is the growth rate. Each perturbation ϕ' in (A14)–(A17) is expressed via (A18) in terms of normal modes. Exemplary for the continuity equation, this results in

$$\boldsymbol{\nabla} \cdot \boldsymbol{u}' \equiv \left[\mathrm{i}k_x \hat{u}'_x\,(z) + \mathrm{i}k_y \hat{u}'_y\,(z) + \frac{\partial \hat{u}'_z\,(z)}{\partial z} \right] e^{\mathrm{i}(k_x x + k_y y) + \sigma t} = 0. \tag{A20}$$

For abbreviation, we define

$$U := \hat{u}'_x\,(z)\,, \quad V := \hat{u}'_y\,(z)\,, \quad W := \hat{u}'_z\,(z)\,, \quad \hat{\Theta}'\,(z) = \Theta, \quad D\phi := \frac{\partial\,(\phi)}{\partial z}, \tag{A21}$$

such that (A20) translates to simply

$$\mathrm{i}k_x U + \mathrm{i}k_y V + DW = 0. \tag{A22}$$

Applying this in a similar fashion to (A15) in z and (A16)–(A17), we obtain

$$\sigma\left(D^2 - k^2\right)W = \left(D^2 - k^2\right)^2 W - Rak^2\Theta_f, \tag{A23}$$

$$Pr\sigma\Theta_f = \left(D^2 - k^2\right)\Theta_f + W, \tag{A24}$$

$$Pr\frac{\kappa_f}{\kappa_s}\sigma\Theta_s = \left(D^2 - k^2\right)\Theta_s. \tag{A25}$$

On the other hand, the boundary conditions (A6)–(A11) translate to

$$W\,(z = \pm 1/2) = 0, \tag{A26}$$

$$DW|_{z=\pm 1/2} = 0, \tag{A27}$$

$$\Theta_f\,(z = 1/2) = \Theta_{st}\,(z = 1/2)\,, \tag{A28}$$

$$\Theta_f\,(z = -1/2) = \Theta_{sb}\,(z = -1/2)\,, \tag{A29}$$

$$D\Theta_f|_{z=1/2} = \frac{\lambda_{st}}{\lambda_f} D\Theta_{st}|_{z=1/2}, \tag{A30}$$

$$D\Theta_f|_{z=-1/2} = \frac{\lambda_{sb}}{\lambda_f} D\Theta_{sb}|_{z=-1/2}. \tag{A31}$$

A.4. *Marginally stable state*

The marginally stable state is the one we are looking for, defining neutral stability. Depending on the imaginary part of the growth rate, the system may be in overstability, if for at least one wavenumber $\mathrm{Im}(\sigma) \neq 0$. Otherwise, if all wavenumbers result in an imaginary part of 0, the principle of exchange of stabilities is valid.

Chandrasekhar (1981) has shown that the latter applies for the Rayleigh–Bénard convection set-up. Moreover, Hurle has adapted this to the CHT case, allowing for the application of this principle (Hurle *et al.* 1967). Thus, we can set

$$\mathrm{Re}\,(\sigma) \overset{!}{=} 0 \wedge \mathrm{Im}\,(\sigma) \overset{!}{=} 0 \Rightarrow \sigma \equiv 0. \tag{A32}$$

Applying this to (A23)–(A25) gives us our modelling equations. We can rewrite (A24)

$$\underbrace{Pr\sigma\Theta_f}_{\sigma=0} = \left(D^2 - k^2\right)\Theta_f + W \Leftrightarrow \Theta_f = -\frac{W}{D^2 - k^2} \text{ or } W = -\left(D^2 - k^2\right)\Theta_f, \tag{A33}$$

and insert it into (A23), yielding either an ordinary differential equation for W,

$$\left(\left(D^2-k^2\right)^3+Rak^2\right)W=0 \tag{A34}$$

or, alternatively, for $\varTheta_f$

$$\left(D^2-k^2\right)\left(\left(D^2-k^2\right)^3+Rak^2\right)\varTheta_f=0. \tag{A35}$$

For the solids, in turn,

$$\underbrace{Pr\frac{\kappa_f}{\kappa_s}\sigma\varTheta_s}_{\sigma=0}=\left(D^2-k^2\right)\varTheta_s\Leftrightarrow\left(D^2-k^2\right)\varTheta_s=0. \tag{A36}$$

An interesting aspect of (A34)–(A36) is that the dependence on the Prandtl number Pr cancels out (because we assumed $\sigma\equiv 0$). Furthermore, all three equations are linear ordinary partial differential equations, making them comparatively easy to solve.

A.5. *Solution of the modelling equations*

Dealing with linear ordinary differential equations, an exponential ansatz of the form

$$\phi\,(z)=e^{qz},\quad \phi=\{W,\varTheta_f,\varTheta_{sb},\varTheta_{st}\} \tag{A37}$$

with the free parameter q is usually promising. Starting with the simplest of the three equations for the temperature deviation, that in the solids $\varTheta_{sb,st}$ (A36), we get

$$\left(D^2-k^2\right)\varTheta_s=0\Rightarrow\varTheta_s\,(z)=c_1e^{-kz}+c_2e^{kz}. \tag{A38}$$

At the very top and bottom of the plates, respectively, temperature deviations must be 0 as the temperature is set by virtue of the (external) thermal boundary conditions. Thus, we apply

$$\varTheta_{st}\,(z=1/2+\varGamma_{st})\overset{(A38)}{\Longrightarrow}\quad\varTheta_{st}\,(z)=c_1\left(e^{-kz}-e^{kz}e^{-k(1+2\varGamma_{st})}\right), \tag{A39}$$

$$\varTheta_{sb}\,(z=-\,(1/2+\varGamma_{sb}))\overset{(A38)}{\Longrightarrow}\varTheta_{sb}\,(z)=c_2\left(e^{kz}-e^{-kz}e^{-k(1+2\varGamma_{sb})}\right). \tag{A40}$$

Solving (A34) and (A35) with this the exponential ansatz leads to

$$\left(\left(q^2-k^2\right)^3+Ra\,k^2\right)W=0, \tag{A41}$$

$$\left(q^2-k^2\right)\left(\left(q^2-k^2\right)^3+Ra\,k^2\right)\varTheta_f=0 \tag{A42}$$

whereas we obtain

$$\varTheta_f=\frac{\left(q^2-k^2\right)^2}{Rak^2}W \tag{A43}$$

using (A23) when setting $\sigma=0$ and using the same exponential ansatz. We obtain the solutions

$$q_{1,5}=\pm\sqrt{k^2-\left(Ra\,k^2\right)^{\frac{1}{3}}}, \tag{A44}$$

$$q_{2,6}=\pm\sqrt{k^2+1/2\left(Ra\,k^2\right)^{\frac{1}{3}}\left(1-\mathrm{i}\sqrt{3}\right)}, \tag{A45}$$

$$q_{3,7} = \pm\sqrt{k^2 + 1/2\left(Ra\, k^2\right)^{\frac{1}{3}}\left(1 + \mathrm{i}\sqrt{3}\right)}, \tag{A46}$$

$$q_{4,8} = \pm k, \tag{A47}$$

where $q_{4,8}$ applies to (A42) only whereas the other solutions are valid for both (A41) and (A42).

Looking at the $(q^2 - k^2)$-term in (A41) and (A42), one can observe symmetry. Therefore, the solution may be written as a combination of sinh and cosh with orthogonal basis functions, splitting the overall solution into the even and odd solutions

$$W = W_e + W_o = \sum_{j=1}^{3} A_j \cosh\left(q_j z\right) + \sum_{j=1}^{3} B_j \sinh\left(q_j z\right), \tag{A48}$$

$$\varTheta_f = \varTheta_{f,e} + \varTheta_{f,o} = \sum_{j=1}^{4} C_j \cosh\left(q_j z\right) + \sum_{j=1}^{4} D_j \sinh\left(q_j z\right), \tag{A49}$$

$$\varTheta_f = \frac{1}{Ra\, k^2}\left(\sum_{j=1}^{3} A_j\left(q_j^2 - k^2\right)^2 \cosh\left(q_j z\right) + \sum_{j=1}^{3} B_j\left(q_j^2 - k^2\right)^2 \sinh\left(q_j z\right)\right), \tag{A50}$$

where (A43) is used to obtain (A50).

A.6. *Applying the boundary conditions*

Now we apply the boundary conditions (A26)–(A31) to solve (A48) and (A49) while using these conditions for the solids (A39) and (A40). For each condition, (A48) and (A49) are split into even and odd modes and solved separately. Regarding identical bottom and top plates, we can further set

$$\lambda_{st} = \lambda_{sb} = \lambda_s, \tag{A51}$$

$$\varGamma_{st} = \varGamma_{sb} = \varGamma_s. \tag{A52}$$

Note that this makes the boundary conditions for the solid bottom domain obsolete as the solution coincides with that of the solid top domain by virtue of symmetry. For (A26), one obtains

$$W_e\left(z = 1/2\right) = \sum_{j=1}^{3} E_j = E_1 + E_2 + E_3 = 0, \tag{A53}$$

$$W_o\left(z = 1/2\right) = \sum_{j=1}^{3} O_j = O_1 + O_2 + O_3 = 0, \tag{A54}$$

with the new constants

$$E_j := A_j \cosh\left(\frac{q_j}{2}\right), \tag{A55}$$

$$O_j := B_j \sinh\left(\frac{q_j}{2}\right). \tag{A56}$$

Applying (A27) yields

$$DW_e\left(z = 1/2\right) = \sum_{j=1}^{3} E_j q_j t_j = 0, \tag{A57}$$

$$DW_o\,(z=1/2)=\sum_{j=1}^{3} O_j q_j c_j = 0, \tag{A58}$$

with

$$t_j := \tanh\left(\frac{q_j}{2}\right), \tag{A59}$$

$$c_j := \coth\left(\frac{q_j}{2}\right). \tag{A60}$$

For (A28) one gets

$$-E_0\frac{\lambda_f}{\lambda_s}\tanh\,(k\varGamma_s)+\frac{1}{Ra\,k^2}\sum_{j=1}^{3}E_j\left(q_j^2-k^2\right)^2=0, \tag{A61}$$

$$-O_0\frac{\lambda_f}{\lambda_s}\tanh\,(k\varGamma_s)+\frac{1}{Ra\,k^2}\sum_{j=1}^{3}O_j\left(q_j^2-k^2\right)^2=0, \tag{A62}$$

where the new constant is

$$E_0=O_0:=c_1e^{-k/2}\cdot\frac{\lambda_s}{\lambda_f}\cdot\frac{1-e^{-2k\varGamma_s}}{\tanh\,(k\varGamma_s)}. \tag{A63}$$

Finally, for (A30) one obtains

$$E_0k+\frac{1}{Ra\,k^2}\sum_{j=1}^{3}E_jq_jt_j\left(q_j^2-k^2\right)^2=0, \tag{A64}$$

$$O_0k+\frac{1}{Ra\,k^2}\sum_{j=1}^{3}O_jq_jc_j\left(q_j^2-k^2\right)^2=0. \tag{A65}$$

As a result, we are left with two systems of equations: One for the even modes and one for the odd modes. Together with the parameter

$$\gamma := \left(Rak^2\right)^{-1/3}, \tag{A66}$$

(A64) and (A65) can be written as

$$\underbrace{\begin{pmatrix} 0 & 1 & 1 & 1\\ 0 & q_1t_1 & q_2t_2 & q_3t_3\\ -\frac{\lambda_f}{\lambda_s}\tanh\,(k\varGamma_s) & \gamma & -\frac{\gamma}{2}\left(1-\mathrm{i}\sqrt{3}\right) & -\frac{\gamma}{2}\left(1-\mathrm{i}\sqrt{3}\right)\\ k & \gamma q_1t_1 & -\frac{\gamma}{2}\left(1-\mathrm{i}\sqrt{3}\right)q_2t_2 & -\frac{\gamma}{2}\left(1-\mathrm{i}\sqrt{3}\right)q_3t_3 \end{pmatrix}}_{\boldsymbol{M_E}}\underbrace{\begin{pmatrix}E_0\\E_1\\E_2\\E_3\end{pmatrix}}_{\boldsymbol{E}}=\begin{pmatrix}0\\0\\0\\0\end{pmatrix}, \tag{A67}$$

$$\underbrace{\begin{pmatrix} 0 & 1 & 1 & 1\\ 0 & q_1c_1 & q_2c_2 & q_3c_3\\ -\frac{\lambda_f}{\lambda_s}\tanh\,(k\varGamma_s) & \gamma & -\frac{\gamma}{2}\left(1-\mathrm{i}\sqrt{3}\right) & -\frac{\gamma}{2}\left(1-\mathrm{i}\sqrt{3}\right)\\ k & \gamma q_1c_1 & -\frac{\gamma}{2}\left(1-\mathrm{i}\sqrt{3}\right)q_2c_2 & -\frac{\gamma}{2}\left(1-\mathrm{i}\sqrt{3}\right)q_3c_3 \end{pmatrix}}_{\boldsymbol{M_O}}\underbrace{\begin{pmatrix}O_0\\O_1\\O_2\\O_3\end{pmatrix}}_{\boldsymbol{O}}=\begin{pmatrix}0\\0\\0\\0\end{pmatrix}. \tag{A68}$$

In other words, both the even and odd solutions represent a system of four equations which must be solved at once. Note that the involved q_j, t_j, c_j and γ are defined in (A44)–(A46), (A59), (A60) and (A66), respectively. The trivial solutions, i.e. all constants $E_j, O_j = 0\,\forall\, j \in [1, 4]$, are obvious. To find the non-trivial solution, the determinants of the given coefficient matrices $\boldsymbol{M_E}$, $\boldsymbol{M_O}$ must contract to zero.

In this solution, there are four free variables left: $\varGamma_s$, λ_f/λ_s, k and Ra. This allows us to fix $\varGamma_s$ and λ_f/λ_s to compute the neutral stability curves $Ra(k)$ for the even and odd solutions.

We find that odd solutions are generally more stable than even solutions. In other words, the neutral stability curves from even solution are below those from odd solutions. Hence, we restrict our analysis in the main text, see (3.1), to the solution of (A67).

Appendix B. Convergence of thermal boundary conditions at extreme ratios of thermal diffusivities κ_s/κ_f

In order to validate our CHT set-up – which adds two identical fluid-confining solid plates at the top and bottom of the classically studied fluid layer – we conduct two simulations using extreme $\kappa_s/\kappa_f = \left\{10^{-6}, 10^{6}\right\}$. These parameters are supposed to resemble the idealised Neumann and Dirichlet case, $\kappa_s/\kappa_f \to 0$ and $\kappa_s/\kappa_f \to \infty$, respectively.

For understanding these limits and their consequences, it is helpful to think of our CHT set-up as a thermal circuit with its different involved thermal resistances or conductances (representing, e.g. the different subdomains) (Incopera *et al.* 2007; Vieweg *et al.* 2025). If one pathway of heat transfer offers a significantly smaller thermal resistance R_{th} – or, as $R_{th} \sim \lambda^{-1} \sim \kappa^{-1}$, larger thermal conductivity or diffusivity – it represents a shortcut and will be favoured over other pathways.

In case of $\kappa_s/\kappa_f \to 0$ or $\kappa_\text{s} \ll \kappa_\text{f}$, the thermal resistance of the solid plates is enormous. However, as our domain is horizontally periodic, heat transfer through these plates is unavoidable and the ‘easiest’ way through the plate is by passing it vertically. This means for the present set-up that heat transfer from T_h to T_c tends to avoid ‘expensive’ horizontal transfer within the solid plates and results in a uniform heat flux at the solid–fluid interfaces. Thus, the classical Neumann case is resembled.

In the opposite case of $\kappa_s/\kappa_f \to \infty$ or $\kappa_\text{s} \gg \kappa_\text{f}$, the thermal resistance of the solid plates is tiny whereas that of the fluid layer is huge. Heat transfer starting from T_h or towards T_c will go all possible ways within the solid plates before eventually interacting with the resistive fluid layer. As a result, heat transfer within the solid plates is faster than through the fluid layer and the plates become isothermal, leading to the classical Dirichlet case.

Figure 12 compares our extreme CHT cases with classical, plateless scenarios. It is obvious that the more natural implementations of the Neumann and Dirichlet cases match their idealised counterparts very well. This first qualitative impression is further confirmed by Nu, Re and $\varLambda_T$ as provided in table 4.

The direct comparison of a plateless Neumann case and the plate-involving CHT case results in an artefact concerning the mean temperature difference across the fluid layer: in the Neumann case, the non-dimensionalisation is not based on the characteristic temperature $T_{char,D} = \Delta T$ (as in the Dirichlet and CHT cases) but rather on the applied vertical temperature gradient across the fluid layer $T_{char,N} = -\partial T/\partial z$. In other words, the characteristic temperature scale is different. As a result, the resulting mean temperature difference $\Delta T_N \leqslant 1$ (Otero *et al.* 2002). This leads to out-of-line scaling in the legend of figure 12 as well as $\max(\varDelta_h T)$ and $\text{std}(T)$ in table 4. However, this is more of a technical issue and can be circumvented by rescaling the solution fields based on ΔT_N (Vieweg

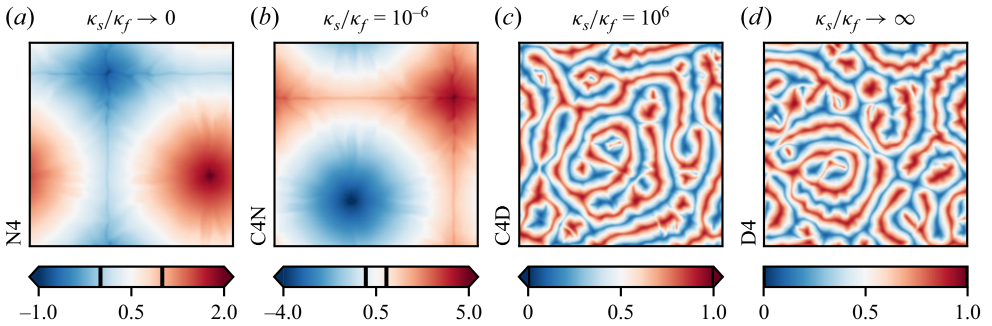

Figure 12. Pattern formation at extreme ratios of thermal diffusivities κ_s/κ_f. For extreme values of κ_s/κ_f, (*b,c*) the flow patterns of CHT simulations converge perfectly towards (*a,d*) those obtained from classical idealised thermal boundary conditions. Here $Ra = 10^4$ and $\Gamma_s = 15$ (if applicable). Note that the simulations from panels (*a,d*) do not comprise any solid plates, whereas those from panels (*b,c*) do.

2023, 2024*a*), eventually realigning the values and proving the validity of our used set-up.

REFERENCES

BÉNARD, H. 1901 Les tourbillons cellulaires dans une nappe liquide transportant de la chaleur par convection en régime permanent. *Ann. Chim. Phys.* **23**, 62–144.

BOUSSINESQ, J.V. 1903 *Théorie Analytique de La Chaleur*. vol. 2. Gauthier-Villars.

CHANDRASEKHAR, S. 1981 *Hydrodynamic and Hydromagnetic Stability*. Dover Publications.

CHAPMAN, C.J. & PROCTOR, M.R.E. 1980 Nonlinear Rayleigh–Bénard convection between poorly conducting boundaries. *J. Fluid Mech.* **101** (4), 759–782.

CHILLÀ, F. & SCHUMACHER, J. 2012 New perspectives in turbulent Rayleigh–Bénard convection. *Eur. Phys. J. E* **35** (7), 58.

CROSS, M. & GREENSIDE, H. 2009 *Pattern Formation and Dynamics in Nonequilibrium Systems*. Cambridge University Press.

FISCHER, P.F. 1997 An overlapping Schwarz method for spectral element solution of the incompressible Navier–Stokes equations. *J. Comput. Phys.* **133** (1), 84–101.

FOROOZANI, N., KRASNOV, D. & SCHUMACHER, J. 2021 Turbulent convection for different thermal boundary conditions at the plates. *J. Fluid Mech.* **907**, A27.

GARCÍA-MELENDO, E., HUESO, R. & SÁNCHEZ-LAVEGA, A. 2013 Atmospheric dynamics of Saturn's 2010 giant storm. *Nat. Geosci.* **6** (7), 525–529.

HORAI, K. 1971 Thermal conductivity of rock-forming minerals. *J. Geophys. Res.* **76** (5), 1278–1308.

HURLE, D.T.J., JAKEMAN, R. & PIKE, E.R. 1967 On the solution of the Bénard problem with boundaries of finite conductivity. *Proc. R. Soc. Lond. A* **296** (1447), 469–475.

IBRAHIM, M.A. & BADAWY, R.B. 2014 A parametric study of the impact of the cooling water site specific conditions on the efficiency of a pressurized water reactor nuclear power plant. *Intl J. Nucl. Energy* **1**, 569658,

INCROPERA, F.P., DEWITT, D.P., BERGMAN, T.L. & LAVINE, A.S. 2007 *Fundamentals of Heat and Mass Transfer*. Wiley & Sons.

JOHNSTON, H. & DOERING, C.R. 2009 Comparison of turbulent thermal convection between conditions of constant temperature and constant flux. *Phys. Rev. Lett.* **102** (6), 064501.

KÄUFER, T., VIEWEG, P.P., SCHUMACHER, J. & CIERPKA, C. 2023 Thermal boundary condition studies in large aspect ratio Rayleigh–Bénard convection. *Eur. J. Mech. B-Fluids* **101**, 283–293.

KOSCHMIEDER, E.L. 1993 *Bénard Cells and Taylor Vortices, Cambridge Monographs on Mechanics and Applied Mathematics*. Cambridge University Press.

KRUG, D., LOHSE, D. & STEVENS, R.J.A.M. 2020 Coherence of temperature and velocity superstructures in turbulent Rayleigh–Bénard flow. *J. Fluid Mech.* **887**, A2.

LONG, R.S., MOUND, J.E., DAVIES, C.J. & TOBIAS, S.M. 2020 Thermal boundary layer structure in convection with and without rotation. *Phys. Rev. Fluids* **5** (11), 113502.

MANNEVILLE, P. 2006 Rayleigh-Bénard convection: thirty years of experimental, theoretical, and modeling work. In *Dynamics of Spatio–Temporal Cellular Structures*, vol. 207, pp. 41–65. Springer Tracts in Modern Physics.

MAPES, B.E. & HOUZE, R.A. 1993 Cloud clusters and superclusters over the oceanic warm pool. *Mon. Weather Rev.* **121** (5), 1398–1416.

MOLLER, S., RESAGK, C. & CIERPKA, C. 2021 Long-time experimental investigation of turbulent superstructures in Rayleigh–Bénard convection by noninvasive simultaneous measurements of temperature and velocity fields. *Exp Fluids* **62** (4), 64.

MOLLER, S. 2022 Experimental characterization of turbulent superstructures in large aspect ratio Rayleigh–Bénard convection. *PhD thesis*, TU Ilmenau.

NIEMELA, J.J. & SREENIVASAN, K.R. 2006 Turbulent convection at high Rayleigh numbers and aspect ratio 4. *J. Fluid Mech.* **557**, 411–422.

OBERBECK, A. 1879 Ueber die Wärmeleitung der Flüssigkeiten bei Berücksichtigung der Strömungen infolge von Temperaturdifferenzen. *Ann. Phys. Chem.* **243**, 271–292.

OCHSNER, T. 2019 *Rain or Shine – An Introduction to Soil Physical Properties and Processes*. Oklahoma State University Libraries.

OTERO, J., WITTENBERG, R.W., WORTHING, R.A. & DOERING, C.R. 2002 Bounds on Rayleigh–Bénard convection with an imposed heat flux. *J. Fluid Mech.* **473**, 191–199.

PANDEY, A., SCHEEL, J.D. & SCHUMACHER, J. 2018 Turbulent superstructures in Rayleigh–Bénard convection. *Nat. Commun.* **9** (1), 2118.

PANDEY, A., KRASNOV, D., SREENIVASAN, K.R. & SCHUMACHER, J. 2022 Convective mesoscale turbulence at very low Prandtl numbers. *J. Fluid Mech.* **948**, A23.

PARODI, A., VON HARDENBERG, J., PASSONI, G., PROVENZALE, A. & SPIEGEL, E.A. 2004 Clustering of plumes in turbulent convection. *Phys. Rev. Lett.* **92** (19), 194503.

PELLEW, A. & SOUTHWELL, R.V. 1940 On maintained convective motion in a fluid heated from below. *Proc. R. Soc. Lond. A* **176** (966), 312–343.

PERELMAN, T.L. 1961 On conjugated problems of heat transfer. *Intl J. Heat Mass Transfer* **3** (4), 293–303.

PLUMLEY, M. & JULIEN, K. 2019 Scaling laws in Rayleigh–Bénard convection. *Earth Space Sci.* **9**, 1580–1592.

RAYLEIGH, L. 1916 On convection currents in a horizontal layer of fluid, when the higher temperature is on the under side. *Lond. Edinburgh Dublin Phil. Mag. J. Sci.* **32** (192), 529–546.

SAMUEL, R.J., BODE, M., SCHEEL, J.D., SREENIVASAN, K.R. & SCHUMACHER, J. 2024 No sustained mean velocity in the boundary region of plane thermal convection. *J. Fluid Mech.* **997**, A49.

SCHEEL, J.D., EMRAN, M.S. & SCHUMACHER, J. 2013 Resolving the fine-scale structure in turbulent Rayleigh–Bénard convection. *New J. Phys.* **15** (11), 113063.

SCHEEL, J.D. & SCHUMACHER, J. 2017 Predicting transition ranges to fully turbulent viscous boundary layers in low Prandtl number convection flows. *Phys. Rev. Fluids* **2** (12), 123501.

SCHINDLER, F., ECKERT, S., ZÜRNER, T., SCHUMACHER, J. & VOGT, T. 2022 Collapse of coherent large scale flow in strongly turbulent liquid metal convection. *Phys. Rev. Lett.* **128** (16), 164501.

SCHINDLER, F., ECKERT, S., ZÜRNER, T., SCHUMACHER, J. & VOGT, T. 2023 Erratum: Collapse of coherent large scale flow in strongly turbulent liquid metal convection. *Phys. Rev. Lett.* **131** (15), 159901.

SCHNEIDE, C., VIEWEG, P.P., SCHUMACHER, J. & PADBERG-GEHLE, K. 2022 Evolutionary clustering of Lagrangian trajectories in turbulent Rayleigh–Bénard convection flows. *Chaos* **32** (1), 013123.

SCHUMACHER, J. & SREENIVASAN, K.R. 2020 Colloquium: Unusual dynamics of convection in the Sun. *Rev. Mod. Phys.* **92** (4), 041001.

STEVENS, R.J.A.M., BLASS, A., ZHU, X., VERZICCO, R. & LOHSE, D. 2018 Turbulent thermal superstructures in Rayleigh–Bénard convection. *Phys. Rev. Fluids* **3** (4), 041501.

STOUT, J.W. & ROBIE, R.A. 1963 Heat capacity from 11 to 300°K, entropy, and heat of formation of Dolomite. *J. Phys. Chem.* **67**, 2248–2252.

TAKEHIRO, S.-I., ISHIWATARI, M., NAKAJIMA, K. & HAYASHI, Y.-Y. 2002 Linear stability of thermal convection in rotating systems with fixed heat flux boundaries. *Geophys. Astro. Fluid Dyn.* **96** (6), 439–459.

VASIL'EV, A.Y., KOLESNICHENKO, I.V., MAMYKIN, A.D., FRICK, P.G., KHALILOV, R.I., ROGOZHEKIN, S.A. & PAKHOLKOV, V.V. 2015 Turbulent convective heat transfer in an inclined tube filled with sodium. *Tech. Phys.* **60** (9), 1305–1309.

VERZICCO, R. 2002 Sidewall finite-conductivity effects in confined turbulent thermal convection. *J. Fluid Mech.* **473**, 201–210.

VERZICCO, R. 2004 Effects of nonperfect thermal sources in turbulent thermal convection. *Phys. Fluids* **16** (6), 1965–1979.

VERZICCO, R. & SREENIVASAN, K.R. 2008 A comparison of turbulent thermal convection between conditions of constant temperature and constant heat flux. *J. Fluid Mech.* **595**, 203–219.

VIEWEG, P.P., SCHEEL, J.D. & SCHUMACHER, J. 2021 Supergranule aggregation for constant heat flux-driven turbulent convection. *Phys. Rev. Res.* **3** (1), 013231.

VIEWEG, P.P., SCHNEIDE, C., PADBERG-GEHLE, K. & SCHUMACHER, J. 2021*a* Lagrangian heat transport in turbulent three-dimensional convection. *Phys. Rev. Fluids* **6** (4), L041501.

VIEWEG, P.P., SCHEEL, J.D., STEPANOV, R. & SCHUMACHER, J. 2022 Inverse cascades of kinetic energy and thermal variance in three-dimensional horizontally extended turbulent convection. *Phys. Rev. Res.* **4** (4), 043098.

VIEWEG, P.P. 2023 Large-scale flow structures in turbulent Rayleigh–Bénard convection: dynamical origin, formation, and role in material transport. *PhD thesis*, TU Ilmenau.

VIEWEG, P.P., KLÜNKER, A., SCHUMACHER, J. & PADBERG-GEHLE, K. 2024 Lagrangian studies of coherent sets and heat transport in constant heat flux-driven turbulent Rayleigh–Bénard convection. *Eur. J. Mech. B-Fluids* **103**, 69–85.

VIEWEG, P.P. 2024*a* Supergranule aggregation: a Prandtl number-independent feature of constant heat flux-driven convection flows. *J. Fluid Mech.* **980**, A46.

VIEWEG, P.P., KÄUFER, T., CIERPKA, C. & SCHUMACHER, J. 2025 Digital twin of a large-aspect-ratio Rayleigh–Bénard experiment: role of thermal boundary conditions, measurement errors and uncertainties. *Flow* **5**, E4.

WONDRAK, T., SIEGER, M., MITRA, R., SCHINDLER, F., STEFANI, F., VOGT, T. & ECKERT, S. 2023 Three-dimensional flow structures in turbulent Rayleigh–Bénard convection at low Prandtl number $Pr = 0.03$. *J. Fluid Mech.* **974**, A48.

WRIGHT, S. 1921 Correlation and causation. *J. Agric. Res.* **20**, 557–585.

YOUNG, R. & READ, P. 2017 Forward and inverse kinetic energy cascades in Jupiter's turbulent weather layer. *Nat. Phys.* **13** (11), 1135–1140.